

UNCLASSIFIED

SECURITY CLASSIFICATION OF THIS PAGE

REPORT DOCUMENTATION PAGE

1a. REPORT SECURITY CLASSIFICATION Unclassified		1b. RESTRICTIVE MARKINGS	
2a. SECURITY CLASSIFICATION AUTHORITY		3. DISTRIBUTION/AVAILABILITY OF REPORT Approved for public release; distribution is unlimited.	
2b. DECLASSIFICATION/DOWNGRADING SCHEDULE			
4. PERFORMING ORGANIZATION REPORT NUMBER(S) TR 7775		5. MONITORING ORGANIZATION REPORT NUMBER(S)	
6a. NAME OF PERFORMING ORGANIZATION Dr. David Middleton	6b. OFFICE SYMBOL (If applicable)	7a. NAME OF MONITORING ORGANIZATION	
6c. ADDRESS (City, State, and ZIP Code) 127 E. 91 Street New York, NY 10128		7b. ADDRESS (City, State, and ZIP Code)	
8a. NAME OF FUNDING/SPONSORING ORGANIZATION Naval Underwater Systems Center	8b. OFFICE SYMBOL (If applicable) Code 10	9. PROCUREMENT INSTRUMENT IDENTIFICATION NUMBER N00140-83-DSK59 (DO-N 403) [also based in part on: N00140-84-M-NM82; N66604-85-B09j]	
8c. ADDRESS (City, State, and ZIP Code) New London, CT 06320		10. SOURCE OF FUNDING NUMBERS	
		PROGRAM ELEMENT NO	PROJECT NO
		TASK NO	WORK UNIT ACCESSION NO.
11. TITLE (Include Security Classification) A PROPOSED SOLITON MECHANISM IN WIND-WAVE SURFACE GENERATION AND SCATTERING			
12. PERSONAL AUTHOR(S) Dr. David Middleton			
13a. TYPE OF REPORT Technical Report	13b. TIME COVERED FROM 11/85 TO 6/86	14. DATE OF REPORT (Year, Month, Day) 1986 December 19	15. PAGE COUNT 58
16. SUPPLEMENTARY NOTATION			
17. COSATI CODES		18. SUBJECT TERMS (Continue on reverse if necessary and identify by block number)	
FIELD	GROUP	SUB-GROUP	
		Soliton, soliton surface; drift-layer, nonlinear wind-wave interaction; backscatter anomalies, nondispersive surface wave motion; surface tension; doppler shift	
19. ABSTRACT (Continue on reverse if necessary and identify by block number) Initially, to account for observed discrepancies in acoustic backscatter strengths and doppler shifts [1]-[3]; [6]-[8], and subsequently, to provide a plausible model of local wind-wave surface generation, a soliton mechanism has been proposed, which appears to play a critical rôle under the following operating conditions: small grazing angles, high frequencies, and moderate to strong wind speeds, in "bubble-free" régimes [3]-[8]. Earlier versions [1]-[3] of the proposed "soliton surface," which is postulated to be a part of the wind-generated surface drift layer, are extended in this study to include the effects of surface tension, as well as many physical and analytical features only outlined in [8]. Surface tension is a dominant factor, setting a minimum thickness, h_{e-min} , of 5.5 mm, to the effective drift layer or "channel" which supports the soliton ensemble. Layer thickness $O(7-8 \text{ mm})$ and soliton speeds $O(30 \text{ cm/s})$ appear typical at (mean) near-surface wind speeds $U_{\infty} \sim 10 \text{ m/s}$. Key features of these solitons (or			
20. DISTRIBUTION/AVAILABILITY OF ABSTRACT <input checked="" type="checkbox"/> UNCLASSIFIED/UNLIMITED <input type="checkbox"/> SAME AS RPT. <input type="checkbox"/> DTIC USERS		21. ABSTRACT SECURITY CLASSIFICATION UNCLASSIFIED	
22a. NAME OF RESPONSIBLE INDIVIDUAL Dr. David Middleton		22b. TELEPHONE (Include Area Code) (203) 440-4877	22c. OFFICE SYMBOL 10

19. (Continuation)

hydraulic "bumps" = one-sided "waves"), which comprise the high wavenumber components of the total surface, including the gravity-capillary structure on which the wind-generated soliton ensemble rides, are: (i) their nondispersive nature, (ii) their independence, reflecting the fact that solitons can travel through one another without distortion; and (iii) that they are (in the present unidimensional models) limiting solutions of the Kortweg-de Vries equation [10].

In addition to accounting for the observed backscatter anomalies and linear doppler shifts, point covariance functions, point-intensity spectra and wavenumber spectra are constructed from the proposed surface model, which exhibit the empirically observed high frequency behavior, i.e., are $O(f_s^{-3})$ and $O(k^{-4})$, as wave frequency (f_s) and wavenumber (k) become large. Extensive experimental support is cited to demonstrate the required nondispersive nature of these wind-generated soliton surfaces, via doppler shift measurements, and to describe the nonlinear wind-wave interactions which ultimately produce the proposed soliton surface.

LIBRARY
RESEARCH REPORTS DIVISION
NAVAL POSTGRADUATE SCHOOL
MONTEREY, CALIFORNIA 93940

NUSC Technical Report 7775
19 December 1986

A Proposed Soliton Mechanism In Wind-Wave Surface Generation and Scattering

✓ David Middleton
Office of the Associate Technical
Director for Technology



Naval Underwater Systems Center
Newport, Rhode Island / New London, Connecticut

Approved for public release; distribution is unlimited.

PREFACE

This work was carried out under NUSC Contract N00140-83-DSK59 (DO-N-403), with Sonalysts, Inc., and in part under NUSC Contract N00140-84-M-MN82, and in part under NUSC Contract N66604-85-BO97 (with Planning Systems, Inc., (PSI) Marine Sciences Division, New London, CT), by Dr. David Middleton, Contractor, 127 E. 91st St., New York, New York, 10128. The Technical Reviewers were Mr. John Chester, NUSC, Code 3331, Dr. Ray Deavenport, NUSC, Code 3332, and Dr. Robert H. Mellen, PSI, New London, CT.

REVIEWED AND APPROVED: 19 DECEMBER 1986


W. A. VON WINKLE
Associate Technical Director for Technology

TABLE OF CONTENTS

List of Figures	ii
List of Principal Symbols	iii
1. Introduction - Background	1
<u>Part I. Analytical Models</u>	
2. The Surface Soliton Model--A Preliminary Formulation.	3
2.1 Canonical Forms	6
2.2 Soliton Solutions	7
2.3 Approximate Wave Forms	10
3. The Soliton Surface Process	13
3.1 The Semi-Isotropic Model	15
3.2 Anisotropic Soliton Surface Models	18
4. Assumptions and Approximations	20
(1) Waveform	21
(2) Pdf of L_0 ($= \eta^{-1} \lambda_0$)	21
(3) Small Excess Speed Assumption ($c_0 \gg \sqrt{v_0}$)	21
(4) Statistical Independence of ζ_0 and L_0	21
(5) Semi-Isotropy	22
(6) Constant Drift Layer Thickness, h_e	23
(7) The "DC" Component of the Soliton Process	24
(8) High-Frequency Behavior	25
<u>Part II. Supporting Experimental Evidence</u>	
5. Backscatter Results	25
5.1 A Check on the Backscattering Data	28
6. Dispersion I: Doppler Experiments and a Proposed Wind-Wave Model	32
6.1 Tank Experiments: Phase Speed and Dispersion	37
6.2 A Proposed Qualitative Wind-Wave Surface Model	41
7. Dispersion II: Mean Doppler Shift	42
8. Doppler Spread	46
9. Conclusions	47
References	R-1

LIST OF FIGURES

2.1	Schematic of a soliton, initiated at (r_j, t_j) , traveling along the line $r(\alpha)$, with speed $c_s = c_0 + v_0$, Eq. (2.21)	9
2.2	Approximations to $\text{sech}^2(2x/L)$, Eq. (2.23).	11
2.3	Pulse shape, "wavelength" $\hat{\lambda}_0$, and width L_0 between e^{-1} points	11
3.1	Geometry of wind direction, wave angle α , Δr , $\Delta\phi$, Eqs. (3.18), (3.19)	19
5.1	Acoustic backscatter geometry; source and receiver at $0_{T,R}$	26
5.2	Incoherent backscatter strengths (Roderick [6], and Galubin [30]) as a function of frequency at small angles and high frequencies in "bubble-free" regimes	27
5.3	Wave-flume point-intensity frequency spectra $W(f_s)$, Mitsuyasu and Honda [20]	29
5.4	Comparison of wave frequency spectra, Mellen, Middleton, and Fitzgerald [8]	30
5.5	Point-intensity spectrum of ocean wave surface, Fig. 7 of Roderick et al. [6]	31
6.1	Experimental arrangement, Mellen [35]	33
6.2	Doppler spectra, Mellen [25]	34
6.3	Phase speed spectra, Mellen [25]	34
6.4	Doppler spectra versus grazing angle, Konrad et al. [36]	35
6.5	Doppler spectra versus azimuthal angle, Konrad et al. [36]	36
6.6	Doppler spectra versus grazing angle, Boehme [37]	36
6.7	Phase speed versus wavenumber, Wright and Keller [28]	37
6.8	Phase speed measurements, Ramamonjarisoa et al. [16]	38
6.9	Wave spectra versus fetch X , Ramamonjarisoa et al. [16]	38
6.10	Surface waveform, Schooley [38]	39
6.11	Drift layer motion, Shemdin [15]	40
6.12	Wind-driven sea surface model, Middleton and Mellen [3]	41
7.1	Doppler shift $-\delta f_0$, as a function of frequency, for the soliton Models I, II, Eqs. (7.2), (7.3), and the classical model, Eq. (7.4), including surface drift and deep current speeds. Theory (Middleton [2], Sec. 3) and experiment, from the data of Roderick et al. [6]	44
8.1	Doppler spread Δf versus frequency (Middleton [2], Sec. 4)	47

LIST OF PRINCIPAL SYMBOLS

A_B	= "overlap" index for soliton process	λ_0	= wavelength of incident acoustic radiation
α	= angle of wave component	$\overline{n_0}$	= average number of solitons per unit path length
a	= wind speed parameter associated with estimated surface drift speeds	ω_s	= angular wave frequency
b	= parameter of approximate waveform	ϕ_{0T}	= azimuthal angle
c_0	= channel propagation speed	ϕ_w	= (mean) wind angle
c_s	= soliton phase speed	R_0	= plane wave reflection coefficient
δ	= delta function	Δr	= path difference
δf_0	= doppler shift	ρ_w	= density of water (g/cm^3)
Δf	= (mean) (rms) doppler spread	S	= shadowing function
η	= wavelength parameter	σ_J	= dispersion constant in KdV equation
f_s	= surface wave frequency	σ_h, σ_s	= soliton process parameters
g	= "gravity" = 980 cm/s^2	J	= surface tension (dynes/cm)
γ_e	= surface dispersion parameter	τ	= $t_2 - t_1$; time difference
h_e	= effective drift layer (or channel) thickness	θ_{0T}	= elevation angle
$h_{e-\text{min}}$	= minimum effective channel thickness	U'_a, U_a, U_∞	= wind speeds
$\hat{i}_s, \hat{i}_x, \hat{i}_y$		$\frac{v}{v_d}$	= mean surface speed of drift layer
$K(\)_S$	= covariance of soliton ensemble	v_c	= deep drift current speed
K_{0S}	= soliton wavenumber	v	= soliton velocity "wave"
k	= wavenumber	$\frac{v_0}{v_{0D}}$	= excess speed of solitons
K_S	= soliton process wavenumber	$\frac{v_0}{v_{0D}}$	= mean doppler speed of waves
\mathcal{L}_0	= basic soliton waveform	W_S	= point-intensity spectrum
L_0	= wavelength parameter	W_2	= wavenumber intensity spectrum
$\hat{\lambda}_0$	= soliton "wavelength"	W_1	= pdf
		X	= moving coordinate; fetch
		$\zeta_0, \zeta, \zeta_x, \zeta_t$	= surface elevations and derivatives
		ζ_S	= soliton ensemble

A PROPOSED SOLITON MECHANISM IN WIND-WAVE SURFACE GENERATION AND SCATTERING*
 DAVID MIDDLETON**

1. Introduction-Background

It has been widely observed that underwater acoustic scattering from wind-wave surfaces is much more intense $O(10-20 \text{ db})$ at small grazing angles $\phi = O(\leq 25^\circ)$, large Rayleigh numbers (the "high-frequency" cases, $f_0 = O(5-30 \text{ kHz, or more})$, and often rather strong mean surface winds $\bar{U}_a = O(5-10 \text{ m/sec})$, than classical scattering models, which are based on a surface combination of gravity and capillary wave components, can predict [1], [2], [3]. In almost all cases up to now it has been suggested that a near-surface bubble mechanism, engendered by foaming or breaking waves, is responsible for the larger observed (acoustic) scattering cross sections [4], [5]. However, the recent, very precise work of Roderick et al. [6], [7] has shown experimentally that these large (backscatter) cross sections occur without significant near-surface bubble structures, under otherwise the same geometric and physical conditions.

A possible surface mechanism which can account for these significantly larger scatter returns, and the observed linear doppler shifts, when bubble structures prove empirically ignorable, has been proposed by Middleton ([1]; [2]). It likewise appears as a critical product in the generation of wind-wave surfaces, in the model proposed by Mellen [cf. Sec. II of [3]], and outlined in [9] and summarized in the supporting evidence cited in Part II ff. The scattering mechanism in question is an ensemble of solitons, or "hydraulic bumps" [9]-[11] (also [12]-[14]), which, in this model, are produced on the wave surface by the interaction of local atmospheric shock waves, with the disturbed wave surface, impinging on a resultant thin wind-driven water surface layer. This latter is a thin $O(\text{millimeters})$ moving surface layer which is developed when a nonzero mean wind speed ($\bar{U}_a > 0$) is established, [15], as the fetch of the sea surface becomes larger [16]. Accordingly, the proposed scattering interface consists of a single wave surface (usually artificially divided into so-called "gravity" and "capillary" wave components), and a truly additional component, namely the soliton "ripples," which now constitute

 *Work supported under NUSC (New London Laboratories) Contract N00140-83-SK59, Delivery Order N 403 (1985), with Sonalysts, Inc., 215 Parkway North, Waterford, CT 06385. [Also based in part on earlier work, supported under NUSC Contracts N00140-84-M-NM 82 and N66604-85-B09.]

**Contractor, Physics and Applied Mathematics, 127 E. 91 St., New York, NY 10128.

the moving wind-driven surface portion, i.e., the wind-drift layer, of the gravity-capillary wave surface [1]-[3], [8].

It has been further shown in [1], [2] that the various analytic approaches and approximations used in earlier analyses of scattering intensities are essentially valid and produce quantitative results which differ little from one another. The observed discrepancies between experiment and theory, therefore, must be attributable to the choice of physical model ([1], [2], Sec. 1, and [17]). In addition, we note that radar data (see [18], [19] and refs. therein) indicate that the level of the wavenumber intensity spectrum of the sea surface (in the ultra-gravity and capillary régimes ($k = 0.5-5(+)$ rad cm^{-1})) depends markedly on the near-surface wind conditions. This means not only \bar{U}_a , but $\text{var } U_a$, etc., namely, all appropriate statistics, say, the first-order pdf of U_a of the turbulent atmosphere, become important for a proper description of the sea surface. Observations made at these wavelengths will depend on the particular spectrum (i.e., sea surface) actually generated. [This point is discussed more fully in [3], Secs. I, III; and [8], and in [19], Fig. 4, [20], Fig. 11, where it is evident that the empirical wave spectrum is unsaturated, and thus dependent on U_a , cf. remarks in [21], Sec. 6, as well.]

Although our proposed model of a surface-layer, wind-produced ensemble of hydraulic solitons has been originally advanced [1]-[3], as a likely candidate mechanism to account for the observed anomalies in underwater acoustic backscatter intensities, this model has both quantitative and qualitative implications which extend to the general wind-wave interaction phenomenon itself, including, for example, surface doppler effects on the one hand and hydrodynamical and oceanographic effects on the other. Since current studies [1]-[3] and particularly [8] have emphasized the empirical aspects of our model, and its (for the most part acoustical) supporting evidence, our principal purpose here is to provide the analytical details, briefly noted elsewhere ([2], [3], [8]). This we do in Part I, while Part II concisely summarizes the supporting evidence, with comparisons of theory and experiment taken from [2] and [8] in particular. (For analytic derivations of the acoustical results, see [2] and references.) In this respect, the present Report is a complement to NUSC Tech. Doc. TD 7583, [8].

Accordingly, this Report is organized as follows: Part I is devoted to the author's proposed analytical model of surface soliton ensembles, with Section 2 providing the elements of the soliton surface model, while Section 3 describes the soliton ensemble process. Section 4 completes the analysis with a discussion of the assumptions and approximations. Part II follows with a concise summary and analysis of the supporting empirical evidence: thus, Section 5 provides a qualitative description of the nonlinear wind-wave-wind interactions which ultimately generate the soliton field on the wave surface, while Section 6 supports the generally non-dispersive character of this field, by showing various pertinent experimental surface doppler shifts. Section 7 further illustrates the model's effectiveness in accounting for the observed backscatter cross sections. Section 8 shows typical observed doppler spreads, and Section 9 completes our study with a short critique and summary, which includes a qualitative comparison of various proposed surface scatter models via their observed doppler and scattering mechanisms. Finally, a number of topics for further investigation are briefly noted.

Part I. Analytical Models

2. The Surface Soliton Model--A Preliminary Formulation

Although we shall ultimately be concerned with sets of solitons, let us begin by considering a single, typical soliton,* moving as part of the thin wind-drift surface layer of the sea surface. Such a soliton, here a "hydraulic bump," is well known to be a limiting solution of the famous Korteweg-de Vries (KdV) equation ([9], pp. 463-468); [10], [11], [13], [14]** here derived by appropriate approximations of the "long-wave" equation (e.g., waves long compared to water depth) in hydrodynamics. We quote Eq. (2.21) of [14], which provides an outline of the procedure, yielding explicitly

*We limit our analysis throughout to one-dimensional solitons. For two-dimensional cases, the Kadomtsev-Petviashvili (KP) equation [42], [43] governs propagation.

**We remark that dimensionality has been removed from the formulations in [11] and [13]; also, in [10], Sec. 5.3, cf. remarks after Eq. (5.3-16). (See also (3.1) of [14], in arriving at Eq. (2.21), and Sec. III therein.)

$$\text{KdV} \Big|_{\text{one-dimensional}}: \boxed{c_0 \zeta_x + \zeta_t + \frac{3}{2} \frac{c_0}{h_e} \zeta \zeta_x + \frac{1}{6} h_e^2 c_0 \zeta_{xxx} = 0,} \quad (2.1)$$

where $c_0 = \sqrt{gh_e}$, $\zeta_x = \frac{\partial \zeta}{\partial x}$, etc., and ζ = water displacement height over reference $\zeta = 0$. Here h_e is the depth of the "channel," or effective thickness of the moving wind-drift layer, of which the typical soliton is part. Equation (2.1), or (2.1a) and its transformations ff., represents a balance of nonlinear forces ($\sim \zeta \zeta_x$), embodying the gravitational force shaping the steepness ($\sim \zeta_x$) of the wave, against dispersive forces ($\sim \zeta_{xxx}$), when there is negligible friction (viscosity) in the fluid.

The KdV equation (2.1) does not, however, include the effects of surface tension, which for these small "ripples" or "bumps" O(mm's) in height, typically, must now be introduced. As Dodd et al. have shown ([10], Section 5.3, and comments following Eq. (5.3-41) therein), surface tension acts to diminish the dispersive forces. Following their approximative procedures (Sec. 5.3), the result is the following (dimensional) KdV equation here:

$$\boxed{c_0 \zeta_x + \zeta_t + \frac{3c_0}{2h_e} \zeta \zeta_x + \left(\frac{c_0 h_e^2}{6} - \frac{J c_0}{2\rho_w g} \right) \zeta_{xxx} = 0,} \quad (2.1a)$$

showing how surface tension, which is ignorable for large solitons, like tidal bores, for example, modifies the KdV equation. Here J is the surface tension (=72.75 dynes/cm at 20°C), ρ_w is the density of water, $\rho_w = 1 \text{ gm/cm}^3$ at 20°C, and $g = 980 \text{ cm/sec}^2$, of course. If we write

$$\boxed{\sigma_J \equiv \frac{c_0 h_e^2}{6} \left(1 - \frac{3J}{\rho_w g h_e^2} \right), \quad c_0 = \sqrt{gh_e},} \quad (2.2)$$

and note that σ_J must be positive for there to be dispersive forces ($\sim \zeta_{xxx}$) balancing the nonlinear forces ($\sim \zeta \zeta_x$) steepening the hydraulic "bump" or "wavelet," then this fact sets a condition on the minimum layer thickness, $h_{e-\text{min}}$, which can support propagation, either of cnoidal waves or solitons, namely

$$\sigma_J > 0 \quad \text{or} \quad h_e > \sqrt{3J/\rho_w g} = h_{e-\text{min}} = 0.47 \text{ cm @ } 20^\circ\text{C}, \quad (2.3)$$

when surface tension is specifically taken into account. We observe that for rather "thick" layers, e.g., $h_e = 5.0$ cm, the coefficient of $c_0 h_e^2/6$ in (2.2) becomes $9.1 \cdot 10^{-3} \ll 1$, so that surface tension effects are negligible, and (2.1) rather than (2.1a) is the proper KdV equation to use in such cases.

By making the simple transformation*

$$v = (3c_0/2h_e)\zeta, \quad (2.4)$$

we obtain from (2.1a) the propagation equation (also a KdV equation) for the excess speed, v , due to nonlinear effects (cf. p. 463, [9]), namely

$$c_0 v_x + v_t + vv_x + \sigma_J v_{xxx} = 0, \quad \sigma_J > 0. \quad (2.5)$$

Using a moving coordinate system where $X = x - c_0 t$, $t' = t$, so that, since

$$\left. \begin{aligned} \frac{\partial}{\partial x} &= \frac{\partial}{\partial X} \frac{\partial X}{\partial x} + \frac{\partial}{\partial t'} \frac{\partial t'}{\partial x}; & \frac{\partial}{\partial t} &= \frac{\partial X}{\partial t} \frac{\partial}{\partial X} + \frac{\partial}{\partial t'} \frac{\partial t'}{\partial t}; \\ \therefore \frac{\partial}{\partial x} &= \frac{\partial}{\partial X}; & \frac{\partial}{\partial t} &= -c_0 \frac{\partial}{\partial X} + \frac{\partial}{\partial t'}; \quad (t' = t), \end{aligned} \right\} \quad (2.6)$$

we see directly that (2.5) reduces to

$$v_t + vv_x + \sigma_J v_{xxx} = 0. \quad (2.7)$$

With the help of (2.4) in (2.7), or using (2.6) directly in (2.1a), we also obtain

$$\zeta_t + \frac{3c_0}{2h_e} \zeta \zeta_x + \sigma \zeta_{xxx} = 0 \quad (2.8)$$

for the KdV equation governing the displacement, $\zeta(x,t)$, now in the moving coordinate system (X,t) .

*This is readily found on starting with (2.7) following, cf. Lighthill ([9], Eq. 96, p. 464), and setting $v = C\zeta$, followed by comparison of the result with (2.8).

2.1 Canonical Forms

For many analyses [10]-[13] it is convenient to develop canonical forms of the KdV equation, which eliminate the explicit dependence on the physical parameters, (c_0 , h_e , σ_J , etc.). For this purpose let us introduce the transformations

$$x' = A(x - c_0 t) = AX; \quad t' = Bt \tag{2.9}$$

in (2.8), so that this relation becomes

$$B\zeta_{t'} + \frac{3c_0}{2h_e} A\zeta_{x'}\zeta + \sigma_J A^3 \zeta_{x'x'x'} = 0, \text{ or} \tag{2.10}$$

$$\zeta_{t'} + \frac{3c_0}{2h_e} \left(\frac{A}{B}\right) \zeta\zeta_{x'} + \sigma_J \left(\frac{A}{B}\right) A^2 \zeta_{x'x'x'} = 0.$$

Next, we choose A/B and A such that:

$$\frac{3c_0}{2h_e} \frac{A}{B} = 6; \quad \sigma_J \left(\frac{A}{B}\right) A^2 = 1, \tag{2.11a}$$

(this is, of course, arbitrary), so that

$$\left. \begin{aligned} A &= \sqrt{3/2h_e^3(1-\gamma_e)}; & B &= c_0 h_e^{-5/2} \sqrt{3/2(1-\gamma_e)} \\ \gamma_e &\equiv 3J/\rho_w g h_e^2; & \therefore \sigma_J &= \sigma_0(1-\gamma_e); & \sigma_0 &\equiv \frac{c_0 h_e^2}{6} \end{aligned} \right\} \tag{2.11b}$$

This puts (2.8) finally in the canonical form

$$\boxed{\zeta_{t'} + 6 \zeta\zeta_{x'} + \zeta_{x'x'x'} = 0.} \tag{2.12a}$$

On setting $\Phi = -\zeta(x',t')$ we reduce (2.12a) to the more familiar canonical relation [11], [13]

$$\left. \begin{aligned} \boxed{\Phi_{t'} - 6\Phi\Phi_{x'} + \Phi_{x'x'x'} = 0}; & \quad x' = \sqrt{\frac{3}{2h_e^3(1-\gamma_e)}} (x - c_0 t) \\ \text{with } \Phi = -\zeta(x',t'); & \quad t' = \frac{c_0 h_e^{-5/2} \sqrt{3}}{\sqrt{2(1-\gamma_e)}} t \end{aligned} \right\} \tag{2.12b}$$

for the KdV equation.

We can also readily show that if ζ is a solution of the KdV Eq. (2.12a), then so also are $\zeta_{t'}$, $\zeta_{x'}$, or $\phi_{t'}$, $\phi_{x'}$, of (2.12b). For example, starting with (2.12a) we have:

$$\begin{aligned}
 & \text{(i). } \frac{\partial}{\partial t'} \text{ of (2.12a): } \zeta_{t't'} + 6\zeta\zeta_{x't'} + 6\zeta_{t'}\zeta_{x'} + \zeta_{t'x'x'x'} = 0 \\
 & \text{(ii). } \underline{\text{if } \zeta_{t'} = \text{sol. of (2.12a)}} \quad \therefore \zeta_{t't'} = 6\zeta_{t'}\zeta_{t'x'} + \zeta_{t'x'x'x'} = 0 \\
 & \text{(iii). Combine (i), (ii): } 6\frac{\partial}{\partial t'}(\zeta\zeta_{x'}) - 6\zeta_{t'}\zeta_{t'x'} = 0 \\
 & \text{(iv). Use (2.12a) for 1st term} \\
 & \quad \text{and (ii) for 2nd term:} \\
 & \quad \frac{\partial}{\partial t'} [\zeta_{t'} + \zeta_{x'x'x'}] - [\zeta_{t't'} + \zeta_{t'x'x'x'}] = 0 \\
 & \quad \text{or } [\zeta_{t't'} + \zeta_{t'x'x'x'}] - [\zeta_{t't'} + \zeta_{t'x'x'x'}] = 0, \\
 & \quad \text{as required (ii): } \zeta_{t'} = \text{sol. of (2.12a)}.
 \end{aligned} \tag{2.13}$$

In a similar way we may proceed for $\zeta_{x'}$, $\phi_{t'}$, $\phi_{x'}$. The importance of this result is that not only are hydraulic "jumps" ($\zeta_{x'}$) solutions of the KdV Eq., but so also are their spatial and temporal derivatives, or hydraulic "bumps," which is what we have here physically. Here ζ represents the surface elevation of a soliton "bump," so that $\int \zeta(dt \text{ or } dx) = Z(t,x)$ is the corresponding "jump," or "dc" impulse solution, cf. Fig. 1, and p. 1444 of [11].

2.2 Soliton Solutions

In general, the soliton solution of (2.12) is obtained by assuming that

$$\begin{aligned}
 \phi(x',t') &= \hat{\phi}(x'-vt'), \quad v = \text{a speed to be determined.} \\
 \zeta(x',t') &= \hat{\zeta}(x'-vt').
 \end{aligned} \tag{2.14}$$

This postulation converts the partial differential equation (2.12b) to an ordinary differential equation:

$$\hat{\zeta}_{x'x'} = v\hat{\zeta} + 3\hat{\zeta}^2; \quad \hat{\zeta}_{x'x'} = d^2\hat{\zeta}/dx'^2, \quad (2.15)$$

long recognized as the differential equation of (the position of) a non-linear pendulum, [9], [14].

The solutions of (2.7) and (2.8), found by the procedures noted above (see also pp. 464, 465 of [9]), are

$$v(x,t) = 3v_0 \operatorname{sech}^2 \left\{ \frac{1}{2} \sqrt{\frac{v_0}{\sigma_J}} [x - (c_0 + v_0)t] \right\}, \quad \sigma_J > 0 \quad (2.16)$$

and directly from (2.4),

$$\zeta(x,t) = \frac{2h_e v_0}{c_0} \operatorname{sech}^2 \left\{ \frac{1}{2} \sqrt{\frac{v_0}{\sigma_J}} [x - (c_0 + v_0)t] \right\}, \quad (2.17)$$

where

$$c_s \equiv c_0 + v_0 = \sqrt{gh_e} + v_0 \quad (2.17a)$$

is the constant soliton speed, with v_0 = the incremental excess speed in the $(X, t'=t)$ coordinate system. [Note that $\hat{v} = Bv$, $\hat{\zeta} = B\zeta$, $B \neq 1$, is not a solution of the KdV Eqs. (2.7), (2.8): the scaling of $\operatorname{sech}^2 \gamma$ in (2.16), (2.17) is not arbitrary.] If we set

$$K_{oS} \equiv \frac{1}{2} \sqrt{\frac{v_0}{\sigma_J}} = \sqrt{3v_0/2c_0 h_e^2 (1-\gamma_e)}, \quad (\text{cm}^{-1}), \quad (2.18)$$

as a kind of characteristic wavenumber, or inverse "wavelength," we can rewrite (2.16), (2.17) somewhat more compactly as

$$\left. \begin{aligned} v(x,t) &= 3v_0 \operatorname{sech}^2 K_{oS}(x-c_s t); & \zeta(x,t) &= \zeta_0 \operatorname{sech}^2 K_{oS}(x-c_s t), \\ \zeta_0 &\equiv 2h_e v_0/c_0 = 2v_0 \sqrt{h_e/g}. \end{aligned} \right\} \quad (2.19)$$

Certain conditions, however, must be obeyed with respect to layer thickness (h_e), amplitude (ζ_0), and "wavelength," $\hat{\lambda}_0 \sim K_{oS}^{-1}$, for solitary solutions to exist, in addition to the basic requirement that the

dispersive forces are nonvanishing, e.g., $\sigma_j > 0$, cf. (2.3). With wavelength $\hat{\lambda}_0$ defined as the distance between approximately 2% values of the bump ζ , this condition is

$$\boxed{\zeta_0 \hat{\lambda}_0^2 / h_e^3 \geq 32} \quad ; \quad \underline{a} \text{ (Lighthill)} \equiv \frac{\zeta_{\max} - \zeta_{\text{trough}}}{2} = \frac{\zeta_{\max}}{2} = \frac{\zeta_0}{2} \quad \left. \vphantom{\frac{\zeta_{\max}}{2}} \right\} (2.20)$$

for solitons, cf. Fig. 116 and Eq. (100), [9].

Periodic cnoidal waves are now damped out, and solitons only can recur, p. 465-466, [9]. Equation (2.20), with (2.3), $h_e > 0.47$ cm, when surface tension is critical, as it is in the thin drift layers encountered in our surface model, governs the production of solitons here. As we shall see below (Sec. 4 ff.), the range of allowed numerical values of these structural parameters appears consistent with existing data. Figure 2.1 shows a typical soliton on the wave surface, in direction α , along the line r , traveling at speed $c = c_0 + v_0$ along this line, when initiated at (r_j, t_j) , e.g.,

$$\boxed{\zeta(r-r_j, t-t_j) = \zeta_0 \operatorname{sech}^2 K_{0S} [r-r_j - c_s(t-t_j)]}. \quad (2.21)$$

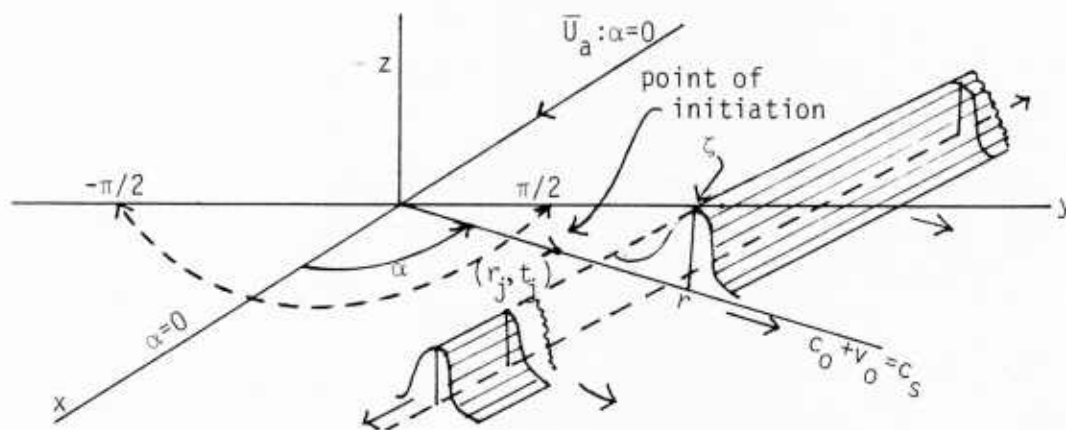


Figure 2.1 Schematic of a (one-dimensional) soliton, initiated at (r_j, t_j) , traveling along the line $r(\alpha)$, with speed $c_0 + v_0 = c_s$, Eq. (2.21).

We note the following important features of the soliton (2.21):

- (1). The effective (two-sided) spread of the hydraulic bump is $\hat{\lambda}_0 \doteq 2bK_{0S}^{-1}n$, (2.24b) ff., which is $\sim v_0^{-1/2}$, i.e., $\hat{\lambda}_0^2 \sim 1/v_0$, cf. (2.17). Thus, the spread is essentially proportional to the depth (or thickness) of the surface layer, h_{eff} .
- (2). The height of the bump, ζ_0 , is $\sim v_0$ and $h_e^{1/2}$, cf. (2.19): thus, the larger v_0 the faster the soliton travels and the larger it is. Also, the thicker the effective layer (h_e), subject to (2.20), the larger is the soliton.
- (3). The larger v_0 , the steeper the bump, i.e., the greater its slope.
- (4). The speed of travel c_s is constant ($v_0 = \text{const.}$) (2.17a), (2.22) so that propagation is nondispersive, a reflection of the fact that dispersive forces are balanced by the nonlinear forces, cf. (2.1), (2.1a).
- (5). Although not obvious here, it can be shown (see [11]) that solitons pass through each other without distortion. This allows us to regard them as mutually independent, when considering them in the ensemble, cf. Sec. 3 ff.
- (6). The solitons represented by (2.16), (2.17) are either generated by a locally plane wavefront, or have traveled a distance from a more local source, i.e., we are assuming here essentially one-dimensional (along a line) propagation.*

2.3 Approximate Wave Forms

The rather complex waveforms for ζ , or v , cf. (2.19), can be greatly simplified for subsequent analysis by approximating them with a simple gaussian "bump." In Figure 2.2, we show the approximation

$$\text{sech}^2(2x/L) \doteq e^{-4x^2/b^2L^2} = e^{-4x^2/L_0^2}; \quad bL = L_0; \quad b = 1.073 \text{ or } 1, \quad (2.23)$$

along with the case $b = 1$, which is also reasonable.

Accordingly, the typical soliton (2.21) is reasonably approximated by

$$\zeta(r-r_j, t-t_j) \doteq \zeta_0 e^{-4|r-r_j-c_s[t-t_j]|^2/L_0^2}, \quad \zeta_0 = 2h_e v_0/c_0, \quad (2.24a)$$

*See footnote, page 3.

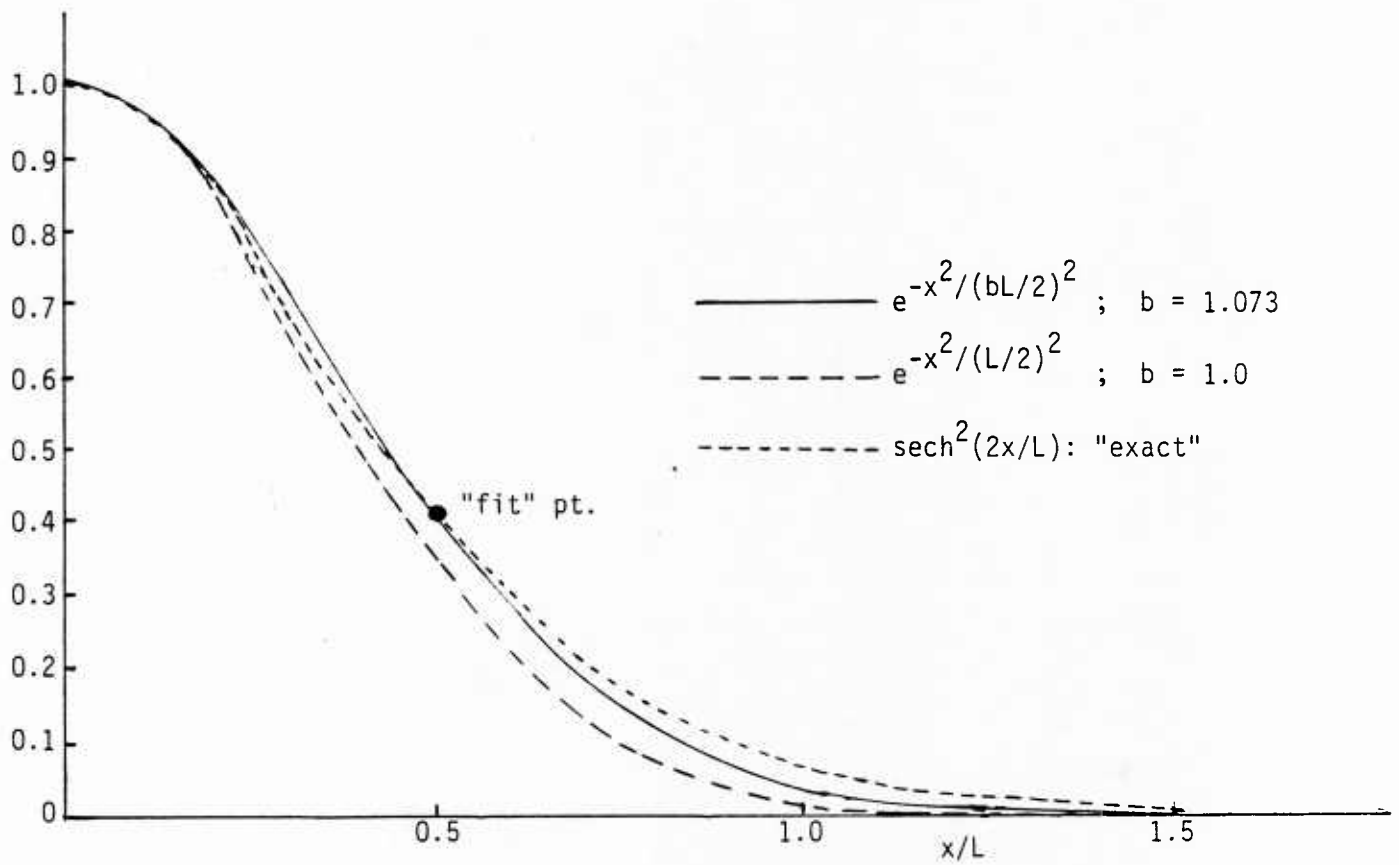


Figure 2.2 Approximations to $\text{sech}^2(2x/L)$, Eq. (2.23).

where now

$$L_0 = 2bK_{OS}^{-1} \text{ and } \hat{\lambda}_0 \equiv nL_0 = 2nb/K_{OS} = 2nb\{2\sqrt{gh}^{5/2}(1-\gamma_e)/3v_0\}^{1/2} \quad (2.24b)$$

from (2.18), with Figure 2.3 showing the relationship between "wavelength" $\hat{\lambda}_0$ and width L_0 between $e^{-\eta^2}$ points.

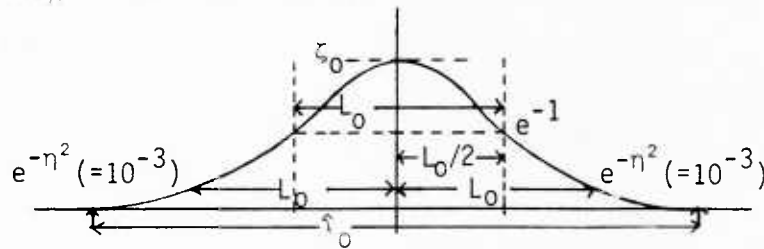


Figure 2.3 Pulse shape, "wavelength" $\hat{\lambda}_0$, and width L_0 between e^{-1} points

[Our choice of η will be made presently, vide (2.29) et seq.] Using (2.4) we see at once that the corresponding form of the excess speed soliton is

$$v(r-r_j, t-t_j) \doteq 3v_0 \exp \{-4|r-r_j-c_s(t-t_j)|^2/L_0^2\}, \quad c_s \doteq c_0+v_0. \quad (2.25)$$

In both cases, (2.23a) and (2.24), we observe that wavelength ($\sim L_0$) depends on layer thickness h_e and on the incremental speed v_0 , cf. (2.17a), (2.23) also. Now the soliton condition (2.20) becomes alternatively, from (2.24b)

$$\boxed{\zeta_0 L_0^2/h_e^3 > 32/\eta^2}, \quad (2.26)$$

in terms of L_0 , the distance between e^{-1} -points, cf. Fig. 2.3.

Next, let us combine the two "existence" conditions: (2.3) for the effects of surface tension, and (2.26), the condition for solitary "waves." The result is a single condition, independent of v_0 , the excess wave speed, for the minimum effective thickness, h_e , of the wind-drift layer, which permits solitons. This is readily found with the help of (2.24a) for ζ_0 and (2.24b) for L_0 , to be

$$\boxed{h_e \geq h_{e-\min} = \left\{ \frac{3J}{\rho_w g (1-2/\eta^2 b^2)} \right\}^{1/2}}, \quad \text{with } (b = 1.073), \quad (2.27)$$

whose numerical value depends, of course, on ηb .

Our next step is to select an appropriate value of η , and hence define the soliton wavelength $\hat{\lambda}_0$, via (2.24b). This is done by first defining the effective channel thickness h_e from the following quasi-physical argument: we require continuity of wave phase speed at the "interface" between the "drift layer" and the underlying gravity-capillary surface, for speeds where surface tension and gravity effects are just equal. This occurs at a minimum phase speed* $c_{s-\min}$, and thus we require that

 *This ties in with $f_{s-\min} \left(= \frac{1}{2} \pi (2g \sqrt{\rho g J})^{1/2} = \frac{84.86}{2\pi} \right) = 13.5 \text{ Hz} \sim$ the empirical 16 Hz resonance of Fig. 6.9, which is larger than $f_{s-\min}$ here because of the wind-drift velocity gradient at the air-water surface, cf. caption, Fig. 4, [16].

$$c_{s-\min} = (4g\tau/\rho_w)^{1/4} = 23.2 \text{ cm/s} = c_{o-\min} = \sqrt{gh_{e-\min}}, \quad (2.28)$$

which accordingly defines $h_{e-\min}$ in our model.

[Here $c_{s-\min}$ is obtained from the general relations $c_s = \sqrt{g(K_S + JK_S^2/\rho_w)}$, $K_S \equiv \omega_s/c_s$, giving $K_{S-\min} = (\rho_w g/J)^{1/2} = 0.364 \text{ cm}^{-1}$, cf. [9], p. 224, Eq. (56).] Using (2.27) in (2.28) accordingly yields the surprisingly simple result

$$\eta b = \sqrt{8}, \quad \text{or } \eta = \sqrt{8}/1.073 = 2.636, \quad (2.29)$$

for our approximating wave from (2.24a). This gives us finally the following set of limiting values (lower bounds) for the existence of solitons associated with the drift layer:

$$h_e \geq h_{e-\min} = \sqrt{4J/\rho_w g} = 0.55 \text{ cm}; \quad c_o \geq c_{o-\min} = 23.1 \text{ cm/s} \quad (2.30a)$$

(@ $\rho_w = 1$, $J = 72.75$ @ 20°C),

$$\therefore \hat{\lambda}_o = 8b\{\sqrt{g} h_e^{5/2} (1-\gamma_e)/3v_o\}^{1/2}, \quad v_o > 0 \quad (2.30b)$$

where again, from (2.11b), $\gamma_e \equiv 3J/\rho_w g h_e^2$, with $(1-\gamma_{e-\min}) = 0.25$, so that $\sigma_J > 0$ in (2.1a), as required.

3. The Soliton Surface Process

The fundamental concept of the soliton surface process is that it represents the decomposition of the actual surface or drift layer into an ensemble of solitons ([9], bottom p. 467; also [13]), whose excess speeds (v_o) and therefore heights and wavelengths are variable quantities, depending on the particular surface produced in the chaotic decay of the wind-wave interaction as fetch is increased (see II of [3], and Sec. 6.1 ff.). Thus, using the approximate form (2.24a), we see that the resulting surface, or "reduced" drift layer, is expressed as a representation of a soliton ensemble by

$$\zeta_S(r, t)_J = \sum_j^J \zeta(r-r_j, t-t_j) = \sum_j^J \zeta_{0j} e^{-4|r-r_j-c_S(t-t_j)|^2/L_{0j}^2} \quad (3.1)$$

where $\zeta_{0j} = \zeta_0(v_{0j})$, $L_{0j} = L_0(v_{0j})$, for a given h_e . The solitons ζ_j comprising this surface ζ_S , represent through (3.1) a decomposition into soliton "components," roughly analogous to a Fourier decomposition.

The soliton ensemble is then $\{\zeta_S\}$, over all allowed values of J .

Our next task is to determine the first- and second-order statistics of ζ_S , in particular, $\langle \zeta_S \rangle$, the covariance $K_S(\Delta r, \tau)$, and associated spectra. To accomplish this, we proceed to make a variety of reasonable statistical assumptions; (see also Sec. 4 ff.). First, we observe that a plausible distribution of values of the L_{0j} is provided by the "half-gaussian" pdf

$$w_1(L_0) = \sqrt{\frac{2}{\pi}} \frac{1}{\sigma_h} e^{-L_0^2/2\sigma_h^2} ; \quad \sigma_h^2 = \overline{L_0^2} ; \quad (\overline{L_0} = \sqrt{\frac{2}{\pi}} \sigma_h). \quad (3.2)$$

Because of the many forces influencing the local surface at r a Central Limit Theorem argument may be invoked to suggest the half-gaussian pdf (3.2) (since $L_0 \geq 0$). Moreover, this pdf favors solitons with lengths shorter than $(\overline{L_0^2})^{1/2} (= \sigma_h)$, although comparatively large values of L_0 ($> \sigma_h$) are not improbable, and, indeed, are needed, to provide significant backscatter returns at the longer Bragg-scatter wavelengths ($\lambda_0/2 \sim 15$ cm, at $f_0 = 5$ kHz; $\lambda_0/2 = 7.5$ cm, at $f_0 = 10$ kHz), cf. Fig. 5.1. [Another, supporting feature of our choice of pdf (3.2) is the perhaps fortuitous fact that it leads to a wavenumber intensity spectrum, $W_2(\underline{k}, 0)_S$, which is $O(k^{-4})$ as k becomes large, cf. Eq. (3.17).]

An important characteristic of solitons is the unusual feature that they remain undistorted when interacting with one another [11], [13]. This suggests that the soliton ensemble, a representation (J) of which is given by (3.1), may be described by a poisson process in space and time, over all points (r_j, t_j) : superposition does not change the individual "wave" forms. Accordingly, we can use recent results [22], [23] to write respectively for the mean and covariance of this poisson process:

$$\langle \zeta_S \rangle = A_B \quad \langle \mathcal{L}_0 \rangle = A_B \int_{-\infty}^{\infty} \langle \mathcal{L}_0(z; \underline{\theta}) \rangle dz \quad \underline{\theta} = L_0, \zeta_0, c_S \quad (3.3)$$

$$K_S = \langle \zeta_{S1} \zeta_{S2} \rangle - \langle \zeta_{S1} \rangle \langle \zeta_{S2} \rangle = A_B \rho_B \int_{-\infty}^{\infty} \langle \mathcal{L}_0(z; \underline{\theta}) \mathcal{L}_1(z + \Delta z; \underline{\theta}) \rangle dz \quad \underline{\theta} = L_0, \zeta_0, c_S \quad (3.4)$$

(with z dimensionless, e.g., $z = y/\overline{L}_0$ here). Because we further postulate local stationarity and homogeneity, $\langle \zeta_S \rangle$ is independent of (r, t) , while $K_S = K_S(\underline{\Delta r}, \tau)$, with $\underline{\Delta r} = r_2 - r_1$; $\tau = t_2 - t_1$ in the usual way. Here A_B represents the "overlap" index for these (Class B) processes ([23], Sec. 3), which in these cases is

$$A_B = \overline{n}_0 \overline{L}_0, \quad \text{with } \rho_B = 1, \quad |\tau| < \infty \left. \vphantom{A_B} \right\} \quad (3.5)$$

$$= 0, \quad |\tau| \rightarrow \infty \left. \vphantom{A_B} \right\} \text{ cf. Eq. (3.5), [23],}$$

where \overline{n}_0 = average number of solitons initiated per unit length (along any line $r-r_j$, cf. Fig. 2.1) and $\overline{L}_0 = \sqrt{\pi/2} \sigma_h$, cf. (3.2), is (proportional) to the mean wavelength $\overline{\lambda}_0 = 2 \overline{L}_0$, (2.23b).

3.1 The Semi-Isotropic Model

We begin with the simplest directional model. For this we assume that all soliton components move in such a way that the covariance K_S depends on $\Delta r = |\underline{\Delta r}| = |r_2 - r_1|$, rather than on $\underline{\Delta r}$. Then the soliton surface field is semi-isotropic, in that all components move downwind, independent of angle, $\Delta\phi$, cf. Fig. 3.1 ff, and Eq. (3.23).

Accordingly, we can write $\Delta y \equiv \Delta r - c_S |\tau|$ for this initial, "semi-isotropic" model and use (2.24a) for ζ_j : i.e., $\mathcal{L}_0 \rightarrow \zeta$ (where all j -parameters have the same pdf's over the ensemble), e.g., specifically,

$$\mathcal{L}_0 = \zeta_0 e^{-4\overline{L}_0^2 z^2 / L_0^2}, \quad z \equiv (r' - c_S t') / \overline{L}_0 = y / \overline{L}_0. \quad (3.6)$$

Putting equation (3.6) into (3.3) then gives

$$\langle \zeta_S \rangle = \left\langle \int_{-\infty}^{\infty} \zeta_0 e^{-4y^2 / L_0^2} dy / \overline{L}_0 \right\rangle_{L_0, \zeta_0} \cdot \overline{n}_0 \overline{L}_0 \quad ; \quad z = y / \overline{L}_0 \quad (3.7a)$$

$$= \frac{\sqrt{\pi}}{2} \overline{n}_0 \overline{\zeta}_0 \overline{L}_0 \quad \doteq \frac{\sqrt{\pi}}{2} \overline{n}_0 \overline{L}_0 \overline{\zeta}_0, \quad |\tau| < \infty. \quad (3.7b)$$

Here we have made the two further assumptions: (i) that ζ_0 and L_0 are essentially independent in the soliton régime, cf. the discussion in (4), Sec. 4 ff., and (ii) that $c_s \approx c_0 = \text{constant}$, i.e., $c_0 \gg v_0$, and $\therefore c_s \doteq \overline{c_s} = c_0 + \overline{v_0}$, cf. (3), Sec. 4. Similarly, we get for (3.4), using (3.6) again:*

$$K_S(\Delta r_1, \tau)_{\text{iso}} = \overline{n_0} \overline{L_0} \left\langle \int_{-\infty}^{\infty} \zeta_0^2 e^{-4y^2/L_0^2 - 4|y+\Delta y|^2/L_0^2} dy/L_0 \right\rangle_{\zeta_0, L_0} \quad (3.8a)$$

$$= \frac{\overline{n_0} \overline{L_0}}{2} \frac{\sqrt{\pi/2}}{2} \left\langle L_0 \zeta_0 \frac{e^{-2\Delta y^2/L_0^2}}{L_0} \right\rangle_{\zeta_0, L_0} \quad (3.8b)$$

$$\doteq \frac{\overline{n_0} \overline{L_0}}{2} \sqrt{\frac{\pi}{2}} \overline{\zeta_0^2} \left\langle (L_0/\overline{L_0}) e^{-2\Delta y^2/L_0^2} \right\rangle_{L_0}, \quad \Delta y \doteq \Delta r - \overline{c_s} \tau, \quad (3.8c)$$

once more with the assumption that ζ_0 and L_0 are independent, cf. Sec. 4. In such cases we have

$$\boxed{K_S(0,0) \equiv \sigma_S^2 = \frac{\overline{n_0}}{2} \overline{L_0} \overline{\zeta_0^2} \sqrt{\frac{\pi}{2}}} \quad (3.9)$$

for the variance of the process. The mean total intensity is

$$\overline{\zeta_S^2} = K_S(0,0) + \langle \zeta_S \rangle^2 \doteq \sigma_S^2 + \frac{\pi}{4} (\overline{n_0} \overline{L_0} \overline{\zeta_0})^2. \quad (3.10)$$

In general, $\overline{\zeta} > 0$, since these solitons are one-sided. However, as we shall note presently, cf. Sec. 4, (6), only the variance σ_S^2 contributes to the effective scattering cross section, since $\langle \zeta_S \rangle$ simply represents a constant vertical displacement of the surface elevation vis-à-vis some reference level, which is arbitrary.

Using (3.2) and the relation

$$\int_0^{\infty} x^{\nu-1} e^{-\beta/x - \gamma x} dx = 2(\beta/\gamma)^{\nu/2} K_{\nu}(2\sqrt{\beta\gamma}), \quad \text{Re } \beta, \gamma > 0, \quad (3.11)$$

[(9), p. 340, [24]], we get for (3.8c) the explicit result for these semi-isotropic cases

*We can drop ρ_B , (3.5), since $K_S \rightarrow 0$, $|\tau|$ or $|\Delta r| \rightarrow \infty$, because of the finite extent of the typical soliton waveform.

$$K_S(\Delta r, \tau)_{iso} = \sigma_S^2 \left| \frac{2\Delta y}{\sigma_h} \right| K_1 \left(\left| \frac{2\Delta y}{\sigma_h} \right| \right), \quad \Delta y \doteq \Delta r - \bar{c}_S \tau, \quad (3.12)$$

(with $\lim_{x \rightarrow 0} xK_1(x) \rightarrow 1$), where K_1 is a modified Bessel function of the second kind. From (3.12) we see at once that the associated point-covariance function is

$$K_S(0, \tau)_{iso} = \sigma_S^2 \left| \frac{2\bar{c}_S \tau}{\sigma_h} \right| K_1 \left(\left| \frac{2\bar{c}_S \tau}{\sigma_h} \right| \right); \quad \sigma_h^2 = L_0^2; \quad \bar{c}_S = c_0 + v_0. \quad (3.13)$$

The associated point-intensity spectrum $W_S(f_S)$ of the soliton surface is now readily obtained from the Weiner-Khintchine theorem ([25], p. 143):

$$W_S(f_S) = 2 \int_{-\infty}^{\infty} K_S(0, \tau) e^{-i\omega_S \tau} d\tau, \quad \omega_S = 2\pi f_S, \quad (3.13a)$$

$$= \frac{2\sigma_h \sigma_S^2}{c_S} \int_0^{\infty} x K_1(x) \cos ax \, dx; \quad a \equiv \omega_S \sigma_h / 2\bar{c}_S \quad (3.13b)$$

$$W_S(f_S) = \frac{\pi \sigma_h \sigma_S^2}{c_S} \cdot \frac{1}{\left[1 + \left(\frac{\omega_S \sigma_h}{2\bar{c}_S} \right)^2 \right]^{3/2}} = \left(\frac{\pi \sigma_h \sigma_S^2}{c_S} \frac{1}{\left[1 + \left(\frac{K_S \sigma_h}{2} \right)^2 \right]^{3/2}} \right), \quad (3.14)$$

since $\omega_S / \bar{c}_S = K_S$, for these nondispersive solitons, where $K_S = 2\pi/\lambda_S$ is the associated (average) wavelength. Note that

$$\int_{0+}^{\infty} W_S(f_S) df_S = \sigma_S^2 :$$

$W_S(f_S)$ is the spectral continuum, exclusive of any "dc"-component $\langle \zeta_S \rangle^2 \delta(f_S - 0)$, cf. (3.10) and (3.7).

Alternatively, from (3.12) we find that for this semi-isotropic model that on setting $\tau = 0$, we get the corresponding spatial covariance function

$$K_S(\underline{\Delta r}, 0)_{\text{iso}} = \sigma_S^2 \left| \frac{2\Delta r}{\sigma_h} \right| K_1 \left(\left| \frac{2\Delta r}{\sigma_h} \right| \right) = K_S(\Delta r, 0), \quad (3.15)$$

which reduces as expected to (3.9) when $\underline{\Delta r} \rightarrow 0$. [Note that (3.15) is independent of the assumption (ii); vide (3), Sec. 4 ff.]

From (3.15) we can obtain the desired wave number intensity spectrum $W_2(\underline{k}, 0)_S$. Noting again the isotropy of our model (3.15), we have specifically

$$\begin{aligned} W_2(\underline{k}, 0)_S &= \iint_{[\underline{\Delta r}]} K_S(\underline{\Delta r}, 0) e^{i\underline{k} \cdot \underline{\Delta r}} d(\underline{\Delta r}) \\ &= 4\pi \sigma_S^2 \sigma_h^{-1} \int_0^\infty J_0(k\Delta r) K_1(2\Delta r/\sigma_h) (\Delta r)^2 d(\Delta r), \end{aligned} \quad (3.16)$$

which from [26], p. 410, Eq. 2 becomes finally

$$W_2(\underline{k}, 0)_S = \frac{\pi \sigma_S^2 \sigma_h^2}{[1 + (k\sigma_h/2)^2]^2} = W_2(k, 0)_S. \quad (3.17)$$

[In backscattering applications, $k = 2k_0 \sin \theta_{OT}$, ($\phi_{OT} = \pi/2$), cf. Sec. 2 and Fig. 2.1 of [2], for example, and (5.1b), Sec. 5 ff.]

3.2 Anisotropic Soliton Surface Models

To handle general anisotropic wind-wave surfaces, we use the well-known relation for the directional covariance of such surfaces [27], extended now from the usual large-scale wave surfaces to include, in principle, our soliton wave surface. The desired relation here is

$$K_S(\underline{\Delta r}, \tau) = \int_0^\infty W_S(f_S) \langle \cos(\omega_S \tau - \underline{k}_S \cdot \underline{\Delta r}) \rangle_\alpha df_S, \quad c_S \doteq \overline{c_S}, \quad (3.18)$$

where now

$$\underline{k}_S = \hat{i}_S K_S = \hat{i}_S \omega_S / \overline{c_S} = \hat{i}_S 2\pi f_S / \overline{c_S}; \quad \hat{i}_S = \hat{i}_X \cos \alpha + \hat{i}_Y \sin \alpha; \quad (3.19a)$$

$$\underline{k}_S \cdot \underline{\Delta r} = K_S \Delta r \cos(\Delta\phi - \alpha); \quad \underline{\Delta r} = \underline{r}_2 - \underline{r}_1; \quad \Delta r = |\underline{\Delta r}|; \quad \Delta\phi = \phi_2 - \phi_1, \quad (3.19b)$$

and where the wind-, soliton "wave", and other geometries are sketched in Figure 3.1. Here

$$\langle \rangle_{\alpha} \equiv \int_{[\alpha]} w_1(\alpha) () d\alpha \quad -\pi/2 \leq \alpha - \phi_w \leq \pi/2, \quad (3.19c)$$

where ϕ_w is the wind angle, for the mean wind direction, $\hat{i}_d = \hat{i}_x \cos \phi_w + \hat{i}_y \sin \phi_w$, and $w_1(\alpha)$ is the pdf of soliton wave directions on the reference (x', y') -surface, cf. Figure 3.1.

Next, we apply (3.14) to (3.18), using the nondispersive relation $\omega_s \doteq \overline{c_s} K_s$ for solitons, cf. (4) of (2.22), to obtain

$$K_s(\underline{\Delta r}, \tau) = B \int_0^{\infty} \left\langle \frac{\cos \omega_s T(\alpha)}{[1 + (a \omega_s)^2]^{3/2}} \right\rangle_{\alpha} df_s; \quad \left. \begin{aligned} T(\alpha) &\equiv \tau - \frac{\Delta r}{\overline{c_s}} \cos(\Delta \phi - \alpha) \\ B &\equiv \pi \sigma_h^2 \overline{c_s}^2 / \overline{c_s} \\ a &\equiv \sigma_h / 2 \overline{c_s} \end{aligned} \right\} (3.20)$$

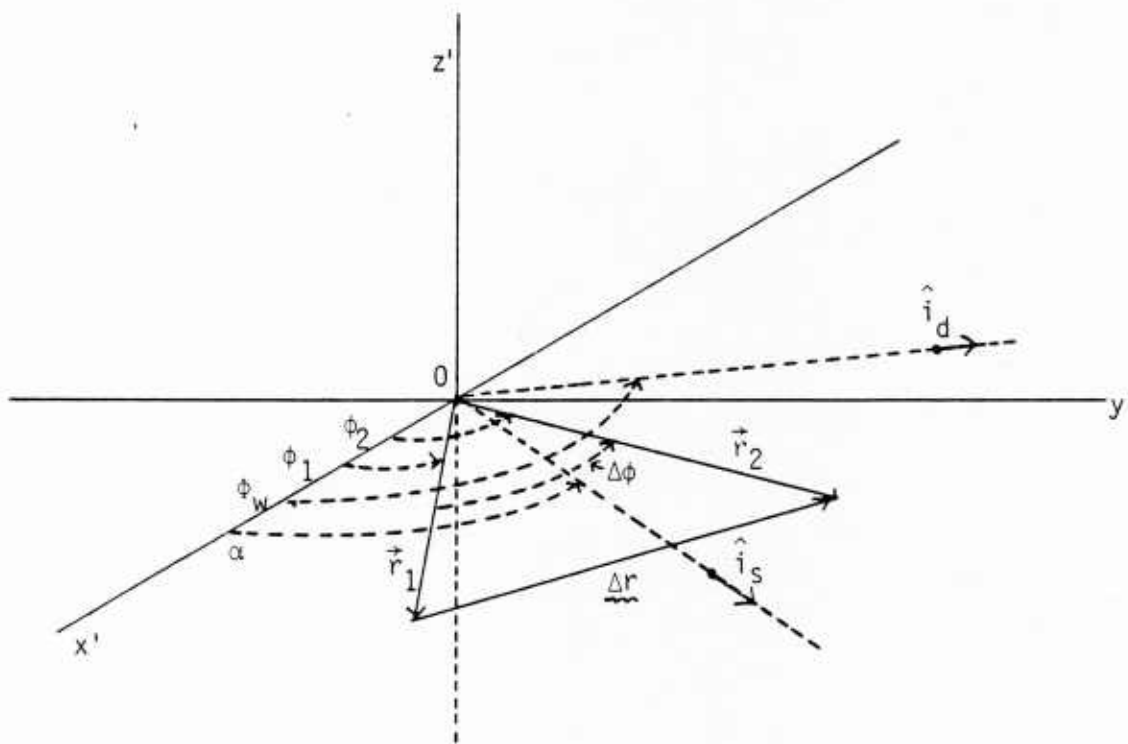


Figure 3.1 Geometry of wind direction, wave angle α , $\underline{\Delta r}$, $\Delta \phi$, Eqs. (3.18), (3.19).

which with the help of (2), p. 426, [24] reduces finally to the general result

$$\boxed{K_S(\Delta r, \tau) = \sigma_S^2 \langle |\beta(\alpha)| K_1(|\beta(\alpha)|) \rangle_\alpha} \quad ; \quad \beta(\alpha) \equiv \frac{2}{\sigma_h} [\overline{c_s} \tau - \Delta r \cos(\Delta\phi - \alpha)], \quad (3.21)$$

Further evaluation of (3.21) depends, of course, on the appropriate choice of $w_1(\alpha)$, which at this stage of our knowledge is unknown. Perhaps a pdf similar to that used for gravity-capillary wave surfaces may be appropriate, viz.,

$$w_1(\alpha) = A_n(f_s) \cos^{n(f_s)} \alpha, \quad -\pi/2 \leq \alpha \leq \pi/2, \quad (3.22)$$

where

$$A_n^{-1} = \int_{-\pi/2}^{\pi/2} \cos^{n(f_s)} \alpha \, d\alpha, \quad (3.22a)$$

cf. Kitaigorodskii [27], Sec. 6.1, and Fig. 2.2 therein, with $n(f_s) \doteq 2$ usually.

For the semi-isotropic model developed above in Section 3.1 we see now that

$$w_1(\alpha) = \delta(\alpha - \Delta\phi) \quad (3.23)$$

for all allowed α , cf. (3.22). Then, $|\beta| = (2/\sigma_h) |\Delta r - \overline{c_s} \tau| = 2|\Delta y|/\sigma_h$, and (3.12) is the directional covariance in this case: $K_S(\Delta r, \tau)$ is independent of direction ($\sim \Delta\phi$), in the downwind régime.

4. Assumptions and Approximations

In achieving our second-order results, e.g., the covariances and spectra of Sec. 3, we have made a series of more or less reasonable approximations and assumptions, whose plausibility needs at least to be discussed.

These are:

(1). Waveform:

From (2.23) we replace the true waveform with a gaussian approximation (2.24a), where, now wavelength $\hat{\lambda}_0$ is defined according to the physical condition (2.28), which is equivalent to the distance between 2% (of maximum) points in the true waveform, cf. (2.24b). This insures a minimum effective channel or drift layer thickness of $h_{e-\min} = 0.55$ cm, cf. (2.30a). The main structure of the soliton waveform is otherwise preserved, in a much simpler form.

(2). Pdf of L_0 ($= \eta^{-1} \hat{\lambda}_0$):

The half-gauss pdf (3.2) for wavelength, or L_0 , is suggested by a Central Limit Theorem argument, as noted above. The critical parameter here is the mean-square, $\langle L_0^2 \rangle$, in any case, regardless of the precise form of the pdf that is chosen. Another supporting feature of this pdf is that it ultimately leads to the wavenumber intensity spectrum (3.17), which has the expected k^{-4} behavior in the higher wavenumbers and leads to an observed f_s^{-3} -dependence in the point intensity spectrum, cf. Figs. 5.3, 5.4 ff., as obtained empirically by Mitsuyasu and Honda [20].

(3). Small Excess Speed Assumption ($c_0 \gg \overline{v_0}$):

In our evaluation here of $\langle \zeta_s \rangle$ and K_s , (3.7), (3.8) we make the important simplifying assumption that $c_0 \gg \overline{v_0}$, so that $c_s \doteq \overline{c_s} = c_0 + \overline{v_0}$, such that we can replace c_s by $\overline{c_s}$ in Δy and in the subsequent analysis (3.8) et seq., independent of v_0 . This is justified if the atmospheric shock waves are "weak" so that the "strength" (β) of the hydraulic jump [associated with the soliton "bump"] is small ($\sim 0.05-0.1$), cf. Sec. 2.12, [9].

(4). Statistical Independence of ζ_0 and L_0 :

In our basic derivations of the mean $\langle \zeta_s \rangle$, (3.7), and covariance, K_s , (3.8c), we have assumed that soliton elevation ζ_0 and wavelength ($\sim L_0$) are independent, when considered over the ensemble of representations ζ_j , (3.1), e.g., $\overline{\zeta_0 L_0} = \overline{\zeta_0} \overline{L_0}$ and $\overline{\zeta_0^2 L_0} = \overline{\zeta_0^2} \overline{L_0}$, even though $\zeta_0 \sim v_0$,

(2.24a), and $L_0 \sim v_0^{-1/2}$, (2.24b). Our justification of this is pragmatic again*: it leads via the covariance (3.12) once more to the point-intensity spectrum (3.14), and associated wavenumber spectrum (3.17), which are empirically supported, cf. Figs. 5.3, 5.4 ff.

(5). Semi-Isotropy:

The soliton field is taken to be (semi-)isotropic, cf. (3.23) and Sec. 3.1, et seq., with soliton motion in the direction of "downwind." This semi-isotropy is probably not often the actual condition: the soliton field is anisotropic, much like that of the gravity-capillary wave surface. However, we expect that numerical differences are subsumed (i.e., disguised) in the various scaling parameters, σ_h , σ_S , and are not distinguishable at the present level of experimental refinement. Again,

*Alternatively, it is possible to find a pdf of the incremental soliton speed v_0 , such that the basic covariance (3.12) is once more obtained, taking into account the fact that now the average with respect to L_0 in (3.8b) is truly an average over v_0 , viz.,

$$\langle c_0^2 L_0 e^{-2\Delta y^2/L_0^2} \rangle_{L_0} = \frac{4Ah_e^2}{c_0^2} \langle v_0^{3/2} \exp(-2v_0 \Delta y^2/A) \rangle_{v_0}; \quad L_0 \equiv A/\sqrt{v_0}, \quad (i)$$

This pdf has the form [under the condition (3) above, viz., $c_0 \gg \overline{v_0}$, with $c_S \rightarrow \overline{c_S} = c_0 + \overline{v_0}$]

$$w_1(v_0) = \left(\frac{3\sqrt{\pi}}{4} a \right)^{-1} (a/v_0)^{7/2} e^{-a/v_0}; \quad a \equiv \left[\langle v_0^{3/2} \rangle \frac{3\sqrt{\pi}}{8} \right]^{2/3} \quad (ii)$$

as determined by the author in an improved model, [41], Secs. 3.1, 3.2. In any case, it is the covariance (3.12) that is fundamental here, as far as the overall statistical structure, e.g., K_S , $W_2(k,0)$, $W_S(f_S)$, etc., is concerned, as suggested by the empirical evidence regarding $W_S(f_S)$, whatever may be the individual structure of the solitons themselves.

these effects need to be isolated in properly controlled experiments.

(6). Constant Drift Layer Thickness, h_e :

The thickness h_e of the effective drift layer is assumed constant for any given developed wind-sea interactions. In fact, in our present model we treat the soliton speed as $c_s = v_0 + c_0$, where now c_0 ($\gg \overline{v_0}$, cf. (3) above) is taken to be the mean surface drift speed, $\overline{v_d}$, so that

$$c_0 = \sqrt{gh_e} = \overline{v_d}, \quad \text{and } c_s \doteq c_0 + \overline{v_0} = \overline{v_d} + \overline{v_0} = \overline{c_s}. \quad (4.1)$$

This follows from the observation here that the solitons are themselves part of the drift layer. The solitons "feel" the bottom of the channel (h_e), and are produced consistent with the strength of the wind-wave interactions, as long as this layer is not so thick that the solitons can no longer sense the effective bottom.

Only v_0 , appearing in the amplitude ζ_0 and wavelength ($\sim L_0$), cf. (4) and footnote, is randomly variable over the ensemble of soliton-surface representations $\{J\}$. The constancy of h_e for a particular, established (i.e., stationary) wind-wave environment, during which the ensemble of soliton-surfaces is generated, appears quite reasonable.

In practice, it has been found that $\overline{v_d}$ and mean wind speed, $\overline{U_a}$ (at some reference height above the mean sea surface) are related rather loosely by

$$\overline{v_d} = a\overline{U_a} = aU_\infty, \quad 0.01 \lesssim a \lesssim 0.05. \quad (4.2)$$

A common choice for a is 3% of $\overline{U_a}$ ($= U_\infty$), but the requirement that $h_e > h_{e-\min}$, (2.30), from (4.1) says that $c_{0-\min} = \sqrt{gh_{e-\min}}$ ($= \overline{v_d}|_{\min}$) = 23.1 cm/sec, so that in our present model mean surface drift speeds must exceed ≈ 23 cm/sec for there to be soliton generation. Moreover, the data of Wright and Keller [28], cf. Fig. 6.7 suggest that for wind speeds $U_\infty = O(8 \text{ m/sec})$ surface wave speed is nearly dispersionless, as required by the soliton model [cf. (4) of (2.22)].

Thus, we must have $\overline{c_s} > 23$ cm/sec, so that if $a \sim 3\%$, $\overline{v_d} = c_0 = 24$ cm/sec (> 23 cm/sec) permits a soliton surface. Even at lower wind speeds, for example, at $U_\infty = 5$ m/sec, Ramamonjariisoa et al. [16], cf. Fig. 6.8, show essentially dispersionless surface wave propagation above about $f_s = 3$ Hz. Here $a = 3\%$ is too small, but $a = 5\%$ gives $\overline{v_d} = c_0 = 25$ cm/sec, permitting

a soliton surface here also. At still smaller values of U_∞ , as Fig. 6.7 shows, surface wave dispersion appears to dominate, so that soliton production is then probably negligible. The precise relation between $\overline{v_d}$ and U_∞ , and hence c_0 and U_∞ , remains to be established here, however, as part of the nonlinear wave and wind interactions, cf. the discussion in Sec. 5 ff.

(7). The "DC" Component of the Soliton Process:

Although the constant elevation component $\langle \zeta_S \rangle$, (3.7b), can be sizeable vis-à-vis the mean square fluctuation, σ_S^2 , (3.9), e.g.,

$$\langle \zeta_S \rangle^2 / \sigma_S^2 = \overline{n_0} \overline{L_0} (\sim 1 \text{ or more}), \quad (4.3)$$

it plays no observable rôle in either the point spectrum (3.14) or wave-number spectrum (3.17). This is because we operate at signal frequencies such that the Bragg scatter occurs at wave frequencies f_S well above "dc." Moreover, direct calculation of the wave number spectrum by using the complete second-moment function

$$M_S(\underline{\Delta r}, 0) = K_S(\underline{\Delta r}, 0) + \langle \zeta_S \rangle^2 \delta(\underline{\Delta r} - 0) \quad (4.4)$$

in

$$\hat{W}_2(k, 0) = \iint_{\underline{\Delta r}} M_S(\underline{\Delta r}, 0) e^{i\mathbf{k} \cdot \underline{\Delta r}} d(\underline{\Delta r}) \quad (4.5a)$$

gives

$$= W_2(k, 0)_{\text{Eq. (3.17)}} + \langle \zeta_S \rangle^2 \int_{-\infty}^{\infty} \int_{-\infty}^{\infty} e^{ik_x \Delta x + ik_y \Delta y} \delta(\Delta x - 0) \delta(\Delta y - 0) d(\Delta x) d(\Delta y)$$

$$\hat{W}_2(k, 0) = W_2(k, 0) + \langle \zeta_S \rangle^2. \quad (4.5b)$$

Again, we operate at frequencies $k > 0$, so that subtracting the constant $\langle \zeta_S \rangle^2$ from $\hat{W}_2(k, 0)$ gives the desired fluctuation term. The $\langle \zeta_S \rangle$ represents a constant vertical displacement from some arbitrary reference level, which can be adjusted to make the contribution of $\langle \zeta_S \rangle^2$ in \hat{W}_2 vanish.

(8). High-Frequency Behavior

From (3.14) and (3.17) we observe the limiting behavior of these spectra as frequency increases. Thus, we have (as f_s and $k \rightarrow \infty$):

$$W_S(f_s) \sim 8\pi c_s^{-2} \left(\frac{\sigma_s}{\sigma_h}\right)^2 \cdot \frac{1}{\omega_s^3}; \quad W_2(k,0)_S \sim 16\pi \left(\frac{\sigma_s}{\sigma_h}\right)^2 \frac{1}{k^4}, \quad (4.6)$$

showing the expected k^{-4} and f_s^{-3} structure. Both spectra exhibit this behavior, in excellent agreement with experiment ([5], [19] for k^{-4} -dependence, for example, Fig. 5.3 here, as well as Fig. 16 of [8], and in [20] for f_s^{-3} -dependence). Of course, ultimately these dependencies must fall off faster, in order to ensure the physically required finite rms slopes. This implies a fall-off at least $O(k^{-5}$ or $f_s^{-4})$, or if fractional exponents are allowed, at least as $O(k^{-4-\epsilon}$ or $f_s^{-3-\epsilon}$, $\epsilon > 0$).

Part II. Supporting Experimental Evidence

To complement the analysis developed in Part I above, we now consider a wide variety of experimental evidence which supports the plausibility of the soliton surface model. To do this, we make extensive use of the description presented in [8], as well as in [3] earlier. Thus, extensive experimental evidence for the soliton scattering mechanism already exists in the open literature and is concisely reviewed here.

5. Backscatter Results

Here we are concerned with the (underwater) acoustic backscatter cross section, where we postulate the surface-soliton component, riding on the gravity-capillary beneath [1]-[3]. The geometry is shown in Fig. 5.1. In particular, small grazing angles and comparatively high frequencies are employed, so that the only significant component of the backscatter is obtained from this soliton surface, as discussed earlier [1]-[3]. Specifically, the Bragg or resonant backscatter cross section is given under these conditions by [1]-[3]

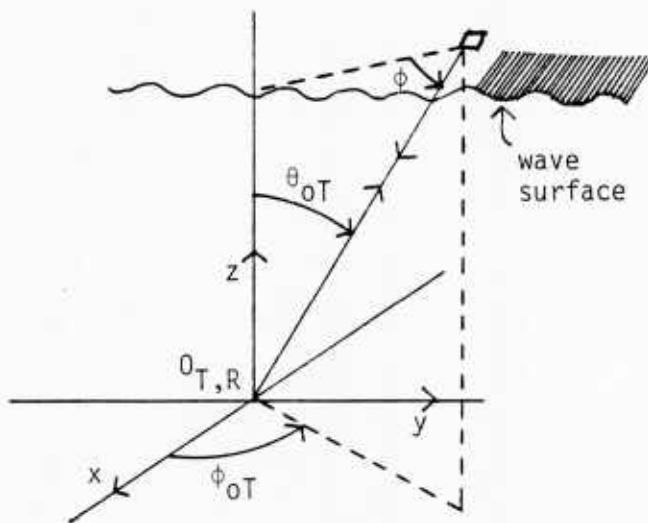


Figure 5.1. Acoustic backscatter geometry; source and receiver at $O_{T,R}$.

$$\hat{\sigma}_{inc}^{(0)} \doteq \frac{\overline{R}_0^2 \overline{S}^2}{16\pi} \frac{k_0^4}{2} N_{GS-inc}^{(0)} W_2(\underline{k}|0), \quad (5.1a)$$

where, from (3.17),

$$\hat{\sigma}_{inc}^{(0)} \doteq \hat{\sigma}_{S-inc}^{(0)} = \frac{2}{\pi} \hat{N}_{GS}^{(0)}(\theta_{OT}) k_0^4 \cdot \frac{\sigma_S^2 \sigma_h^2 / 2}{[1 + (\sigma_h k_0 \sin \theta_{OT})^2]^2}, \quad (5.1b)$$

where $\hat{N}_{GS}^{(0)}$ ($\equiv N_{GS}^{(0)}/16$) is the "tilt factor" ([1], eq. (7.66a), sec. 3.1A), which accounts for the (amplitude) modulation of the small-scale surface waves by the gravity wave component of the surface, in the usual way. Specifically,

$$\left. \begin{aligned} \hat{N}_{GS}^{(0)} \Big|_{\text{backscatter}} &\doteq 3\sigma_{Gx}^4 \sin^4 \theta_{OT} + 6\sigma_{Gx}^2 \sin^2 \theta_{OT} \cos^2 \theta_{OT} + \cos^4 \theta_{OT}, \\ \phi_{OT} &= \pi/2; \quad \sigma_{Gx} = \sigma_{Gy} \end{aligned} \right\} (5.2)$$

where $\sigma_{G(x=y)}^2 = (3.0 + 5.12\overline{U}_a)10^{-3}$ [29]. (The reflection and shadowing

coefficients R_0, S in (5.1) are essentially unity here, e.g., $R_0^2 \doteq S^2 \doteq 1$, as long as $\theta_{OT} < 85^\circ$.)

Backscatter results of experiment and the theory briefly summarized above are presented in Figure 5.2 for $\theta_{OT} = 81^\circ$ ($\phi = 9^\circ$) and $\hat{N}_{GS}^{(0)} = 1.68 \cdot 10^{-2}$, for $\bar{U}_a = 10$ m/s; here $S^2 \doteq R_0^2 \doteq 1$ and a +2.5 db has been added for the Kirchoff correction at these small angles (all curves). The comparison, or more precisely, the fit of theory to experiment is made (for the above geometry) over 5-20 kHz. Narrow-band signal transmission and reception are used by Roderick et al. [6]; explosive charges were employed by Galubin [30] (see also [4], fig. 1.26), with narrow-band

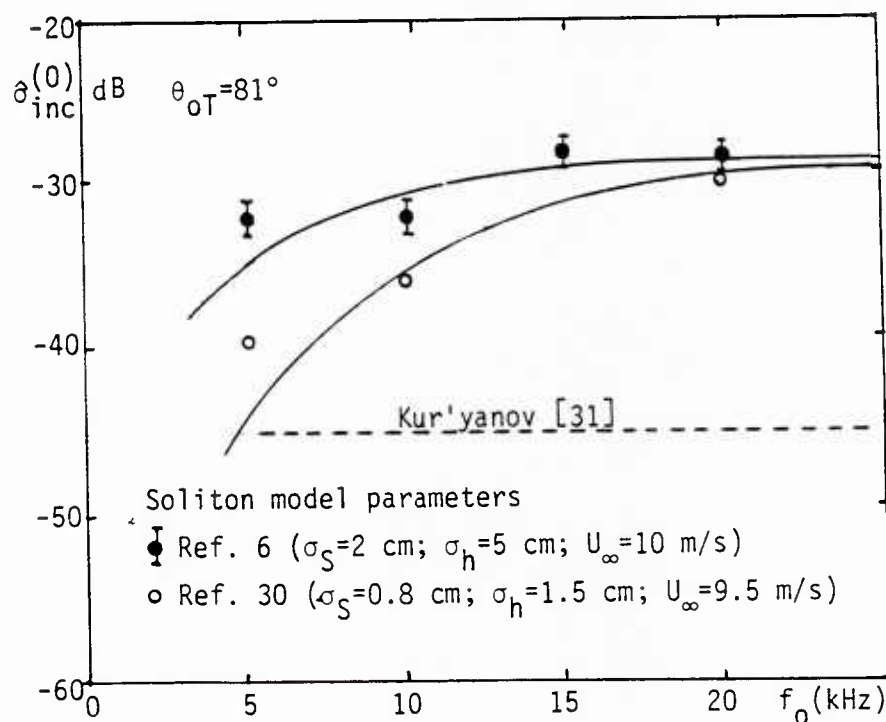


Figure 5.2 Incoherent backscatter strengths (Roderick [6], and Galubin [30]) as a function of frequency at small angles and high frequencies in "bubble-free" régimes. Solid lines: theory [1]-[3].

reception. Figure 5.2 also includes some typical theoretical backscatter cross sections (dotted line), based on purely gravity-capillary surface resonance returns as derived by Kur'yanov's method [31] (see also [4], sec. 9.11, sec. 1.6, p. 203, figs. 1.26, 9.10; [1], eq. (3.18)). In the figure the $\bar{\sigma}$ represent the recent data of Roderick ([6], fig. 10) for coherent pulsed cw signals, while the \circ points are the data of Galubin [30], who used explosive sources. The added soliton component makes up the difference between the "classical" result [31] and the observed cross sections. (See also Sec. 5.3 ff.)

It is evident that although the mean wind speeds $\overline{U_a}$ were essentially the same (~ 20 kn = 10 m/s) in the two cases, different wind states were in force, as quantified by different values of var U_a (and higher moments as well). This is evidenced by the different wavelengths of the solitons ($\sim \sigma_h$) and by the different (rms) soliton levels σ_S . Fetch and wind duration, in addition, are also important factors at the low wave number end of the spectrum, while wind turbulence and drift current can have effect at the higher wave numbers.

With two adjustable scaling parameters, there might appear to be much latitude in curve-fitting; however, the dependence of $\sigma_{inc}^{(0)}$ on mean wind speed, or some related parameter, should be systematic, which it is not here, cf. Fig. 5.2. Moreover, the soliton component can be expected to show critical threshold effects, i.e., vanishing for mean wind speeds less than ~ 2 m/sec and saturating for speeds greater than ~ 10 m/sec. Thus, as noted above, mean wind speed alone is not an adequate parameter and the effects of gusts may also be important. Evidence for this is observed, not only in scattering, but also in ambient noise. Both seem to show variations that are not strictly dependent on mean wind speed.

5.1 A Check on the Backscattering Data

In order to check the plausibility of the model used in matching the backscattering data, it would be useful to have actual wavenumber spectra taken under similar wind conditions as the experiments. Unfortunately, only point-frequency spectra are available for this purpose. Furthermore, measurements made at sea, under appropriate conditions of wind and fetch, do not adequately cover the high-frequency region of

concern. Therefore, laboratory point spectra of elevation will be used for comparison purposes. Thus, to check model plausibility here, the spectrum is simply added to the normal gravity-capillary wave surface spectrum. The backscatter strength is then calculated by composite surface theory, as before.

Figure 5.3 shows wave elevation spectra measured in a wind-wave flume by Mitsuyasu and Honda [20] for 8.25 m fetch and mean wind velocities of 5, 10, 15 m/s. The dashed line is the Pierson-Moskowitz [33] or P-M spectrum for the fully developed equilibrium sea, which is given by:

$$W(f_s)_{P-M} = 2.6 \cdot 10^{-6} g^2 f_s^{-5} \exp(-4.75 \cdot 10^{-4} g^4 f_s^{-4} U_\infty^{-4}), \quad (\text{m}^2/\text{Hz}), \quad (5.3)$$

where $g = 9.8 \text{ m/s}^2$, f_s again (cf. (3.14) et seq.) is the frequency, and U_∞ is mean wind speed. Note that the P-M spectrum is saturated in the frequency range shown, its peaks falling well below 1 Hz (e.g., at $U_\infty = 10 \text{ m/s}$ the peak is at $f_{s\text{-peak}} \approx 0.14 \text{ Hz}$). The data peaks do decrease in

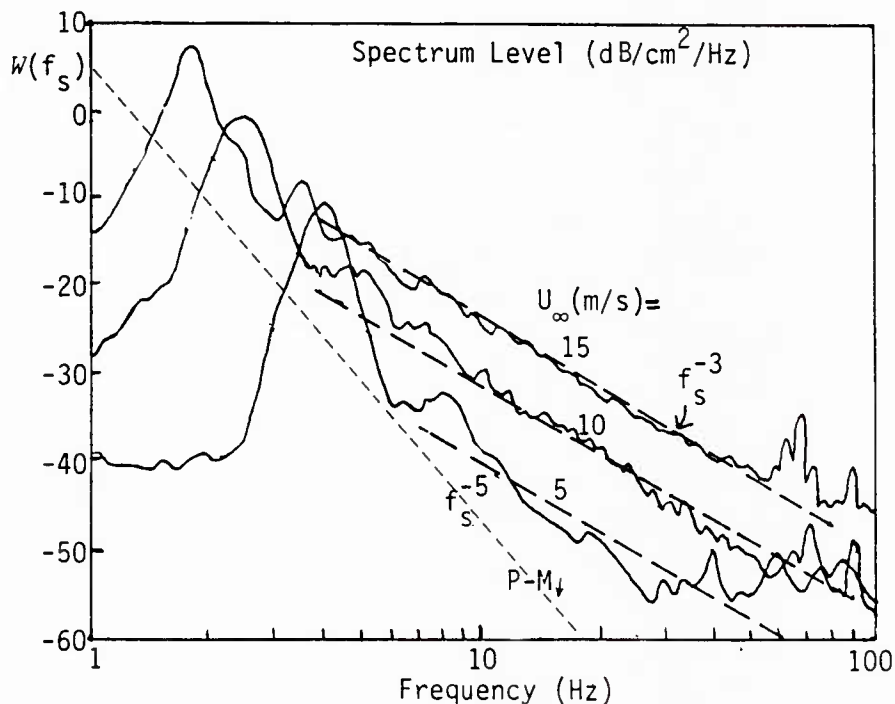


Figure 5.3 Wave-flume point-intensity frequency spectra $W(f_s)$, Mitsuyasu and Honda [20].

frequency with increasing wind speed but the fetch is obviously far too small to approximate the fully developed sea.

Transformation of the P-M asymptote to K-space using the gravity dispersion relation $K_S = (2\pi f_S)^2/g$ (neglecting azimuthal dependence) yields the asymptotic wavenumber spectrum $W_2(K(f_0)) = 6.5 \cdot 10^{-4} K^{-4}$.

At higher frequencies, the data fall well above the P-M asymptote and have roughly f_S^{-3} dependence. Clearly, these wave spectra are unsaturated at the higher frequencies [20], [21], [40]. Without dispersion, $K = 2\pi f_S/C$ where C is a constant and the spectral asymptote would also be K^{-4} . This is precisely the situation indicated in (4.6) above, and is the justification for our requirement that the associated covariance of the elevations have the form (3.13), cf. (4), Sec. 4 also. [The spectra also show several distinct peaks in the range 70-100 Hz, which may be due to the "capillary" ripples noted in Figure 6.10 ff. Effects on scattering are significant only at 100 kHz or greater.]

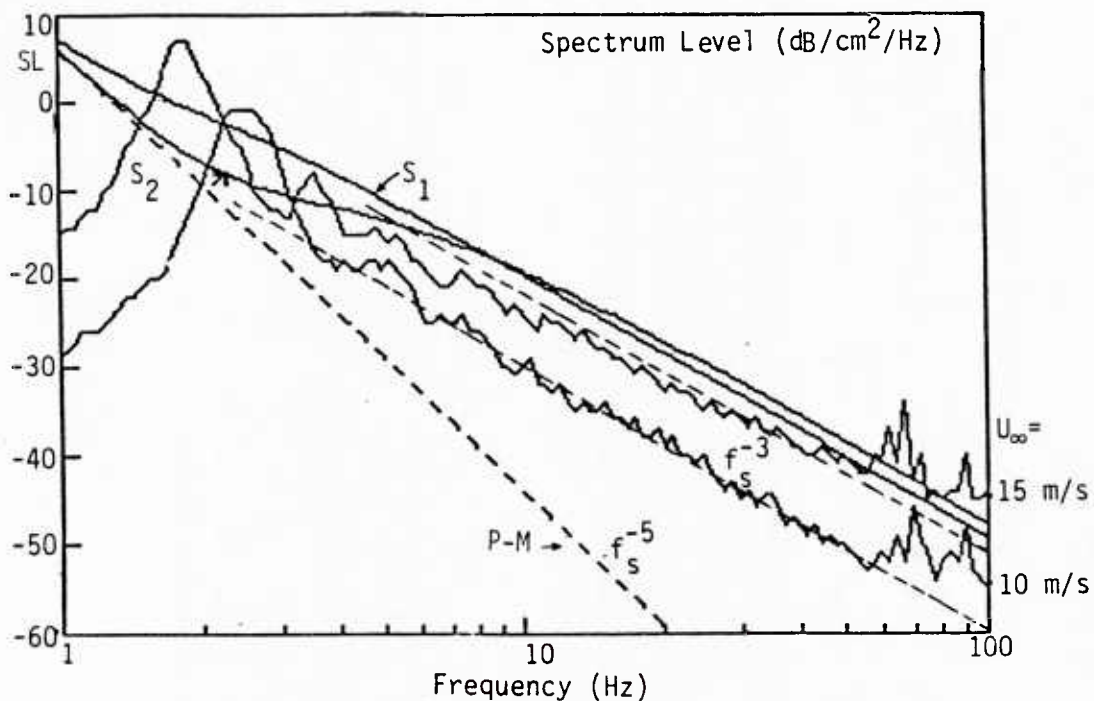


Figure 5.4 Comparison of wave frequency spectra, Mellen, Middleton, and Fitzgerald [8].

Results are summarized in Figure 5.4. The curves labeled 10 and 15 m/s are the spectra of Figure 5.3. The curve P-M is the asymptotic Pierson-Moskowitz spectrum. The spectra S_1 (Roderick et al. [6]) and S_2 (Galubin [30]) indicate addition of the respective soliton components used in the backscatter intensity matching in Figure 5.2 to the P-M spectrum. The soliton components were calculated taking the propagation speed in the fixed-coordinate system to be 50 cm/s, which is in reasonable accord with measured values.

The wind-flume spectra have the same general shape as the model spectra; however, above 10 Hz, the 10 m/s wind-flume curve is lower than the model by as much as 6 dB. This may not be too surprising,

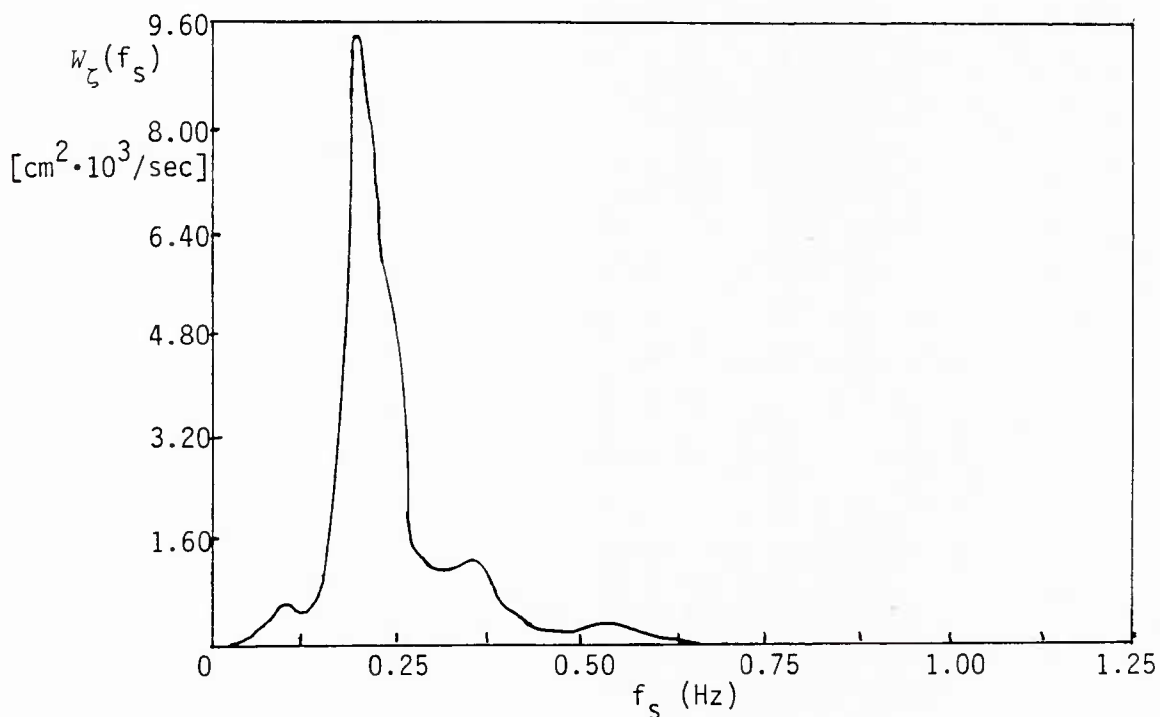


Figure 5.5 Experimental point-intensity spectrum of wave surface, Fig. 7 of Roderick et al. [6].

in view of the very short fetch of the wind-flume experiment. In the backscattering experiments, fetches were of the order of kilometers. In the NUSC experiment (Fig. 7 of [6] and Fig. 5.5 here), for example, the spectral peak occurred at 0.2 Hz, which is much closer to the calculated P-M value $f_{s\text{-peak}} = 1.14$ Hz above. (The difference is explained by the fact that the observed sea was not fully developed.)

The 15 m/s wind-flume spectrum is in much better agreement with the model, indicating that a higher wind-speed may tend to make up for the lack of fetch. We see from this that the present soliton model fitting the various backscatter data also agrees well with the wave frequency spectra, subject to the fetch limitations noted above, i.e., there is sufficient spectral energy to account for the observed backscatter cross sections.

6. Dispersion I: Doppler Experiments and a Proposed Wind-Wave Model

In addition to the discrepancies observed in the backscatter cross sections at small angles and high frequencies for "bubble-free" régimes, discussed above in Sec. 5, anomalous behavior of surface waves was also observed in the doppler spectra. According to classical theory, the cw backscatter spectrum from a narrow acoustic beam should have sharp spectral lines corresponding to Bragg resonance. The dispersion relation for phase speed c_s is given by $c_s^2 = g/K + JK/\rho_w$, where $g = 980 \text{ cm/s}^2$ and J is surface tension ($= 72.75 \text{ dynes/cm}$ at 20°C). This relation was expected to hold over the entire surface-wave spectrum. However, experiment did not support this argument. Instead of the predicted sharp line, a broad peak was observed with a doppler shift quite different from the predicted value.

A doppler experiment in the Thames River by Mellen [35] in 1963, is illustrated in Figure 6.1. In this experiment, the operating frequencies were 85 kHz and 1400 kHz, corresponding to resonance with the surface wavenumbers 5/cm and 40/cm respectively for the grazing angle 45° . The cw signal, backscattered from the illuminated surface, was band-shifted for spectrum analysis and the results plotted as a function of doppler shift δf_0 from the carrier frequency f_0 (Figs. 6.2 and 6.3). The expected doppler shift is given by $\delta f_0 = 2f_0 (c_s/c) \cos \theta_{OT}$, where c is the sound speed.

The mean wind speed for the experiment was estimated to be 10 m/s. Although a few "whitecaps" were noted, there was no evidence of any significant entrapment of air. Pulse measurements showed no subsurface return. Therefore, the observations are believed to be indicative of purely surface-wave phenomena and not bubbles.

Figure 6.2 compares the measured doppler spectra with the expected resonances indicated by the dashed lines. Negative shift corresponds to the downwind conditions of the experiment. Much of the doppler spread can be attributed to modulation by the larger gravity waves. However, the doppler shift at 1400 kHz is much too small.

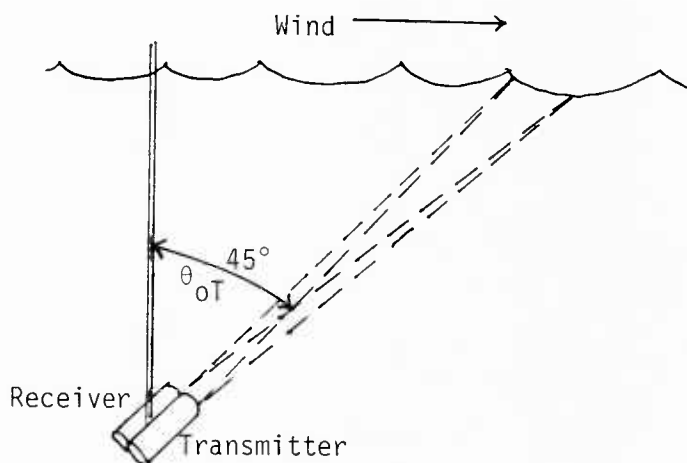


Figure 6.1 Experimental arrangement, Mellen [35] (see also Fig. 5.1).

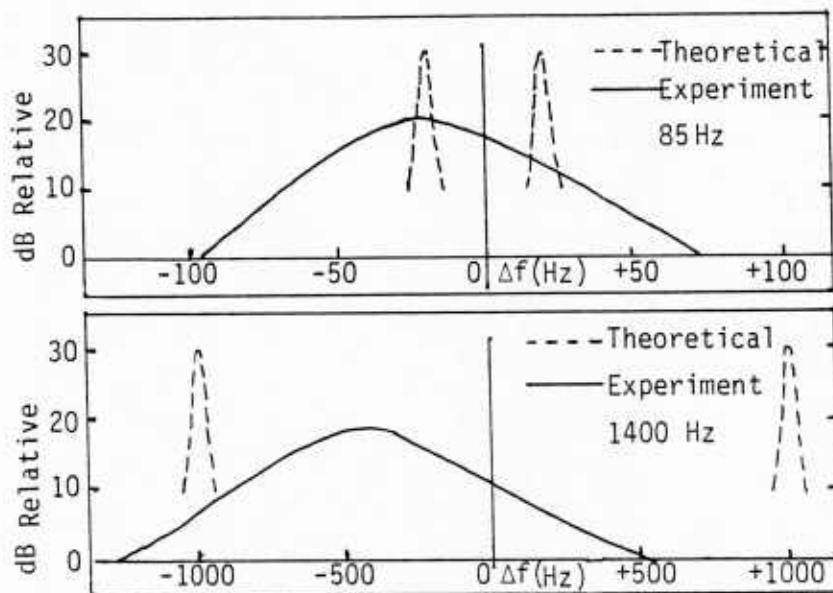


Figure 6.2 Doppler spectra, Mellen [25].

In Figure 6.3, the spectra are scaled according to apparent phase speed. Both spectral peaks then coincide at approximately -35 cm/sec, and this indicates that the scatterers are traveling nondispersively.

The doppler spectra of the Lake Seneca experiments by Konrad et al. [36], Figure 6.4, illustrate the effect of grazing angle looking upwind.

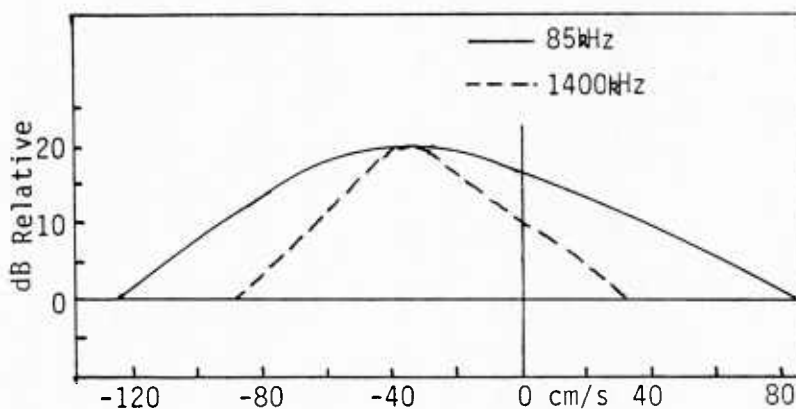


Figure 6.3 Phase speed spectra, Mellen [25].

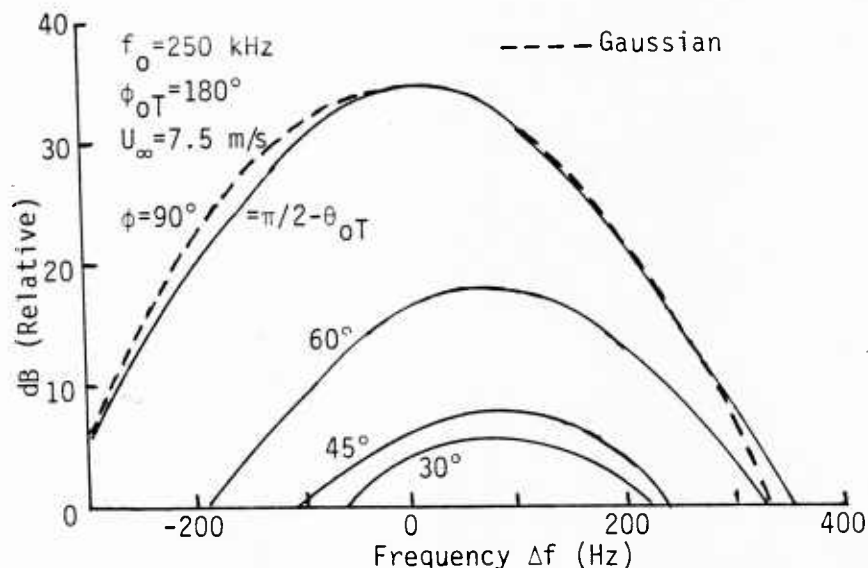


Figure 6.4 Doppler spectra versus grazing angle, Konrad et al. [36].

The relative speed of the scatterers varies as $c_s \sin \theta_{OT}$ and the peak of the spectrum shifts upward by an amount corresponding to $c_s \approx 35$ cm/s.

Normal to the surface ($\phi = 90^\circ$; $\theta_{OT} = 0$), the spectrum becomes symmetric about zero and is very close to gaussian. This is characteristic of gravity waves, and modulation of the scatterers by gravity wave motion must be the dominant factor in spectral spreading. Calculations show that essentially all of the doppler spread is accounted for by this mechanism. The dominant surface-wave angular frequency was estimated to be $\omega_s \approx 3/\text{sec}$. At $\phi = 90^\circ$, the doppler spread around zero for the rms waveheight $\sigma_\zeta \approx 10$ cm is then $\delta f_o = 2f_o f_s \sigma_\zeta / c \approx \pm 100$ Hz, which is in good agreement with experiment.

The shift of the spectral peak with angle is consistent with propagation of the scatterers in the downwind direction independently of the motion of the gravity waves on which they ride. The average downwind speed is approximately 35 cm/sec. Some variability of both speed and direction of propagation is to be expected, but the effect on spectral spreading at large grazing angles should be small.

Variation of angle with respect to wind direction also shifts the spectral peak, as seen in Figure 6.5. Crosswind, the spectrum is symmetrical around zero, as expected.

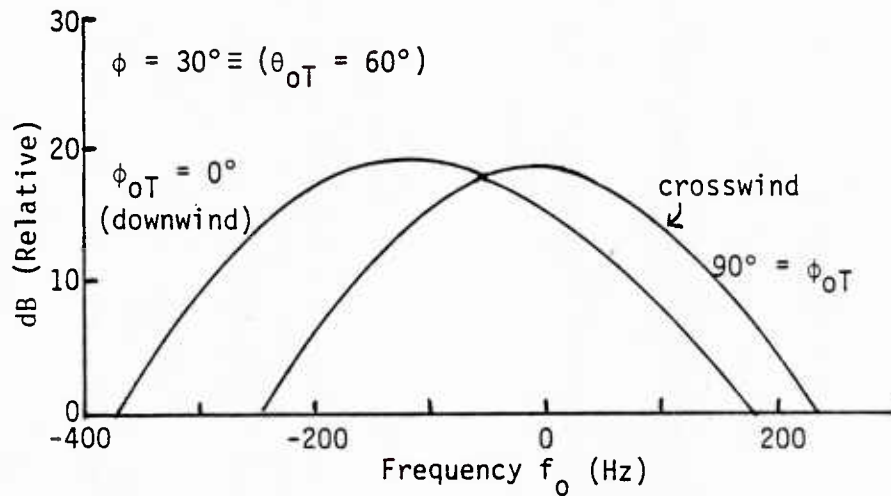


Figure 6.5 Doppler spectra versus azimuthal angle, Konrad et al. [36].

Figure 6.6 shows similar effects observed by Boehme [37] in Lake Travis experiments, looking downwind at the frequency 455 kHz with mean wind speed 4 m/sec. The asymmetry of the spectrum indicates a velocity of ~ 50 cm/sec, which is significantly greater than the other results.

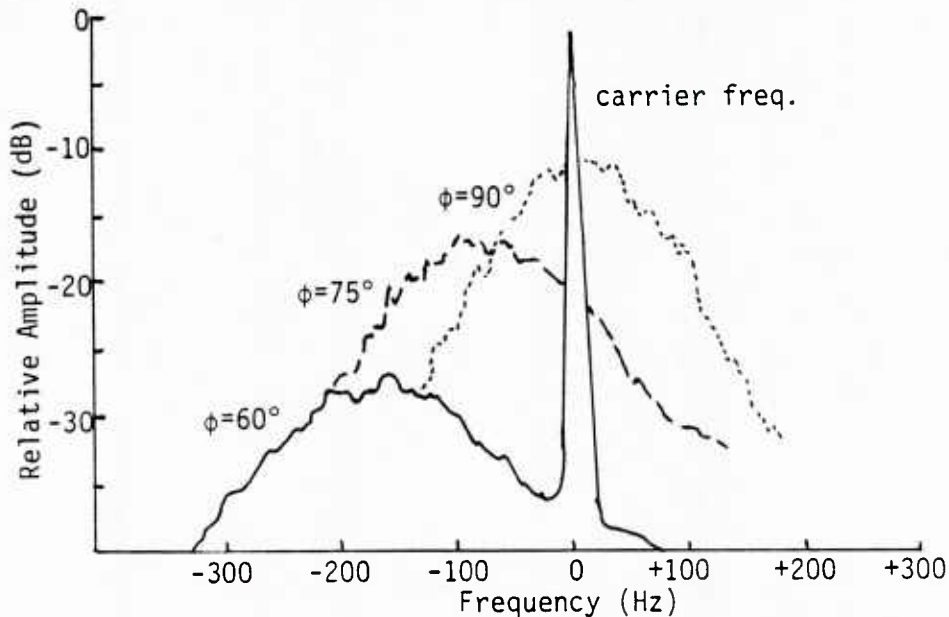


Figure 6.6 Doppler spectra versus grazing angle, Boehme [37].

6.1 Tank Experiments: Phase Speed and Dispersion

In ripple-tank experiments, Wright and Keller [28] used a wave gauge to measure effects of wind on the phase speed of mechanically generated surface waves. Figure 6.7 compares the dispersion formula (solid line) with data, which show negligible dispersion at high wind speeds.

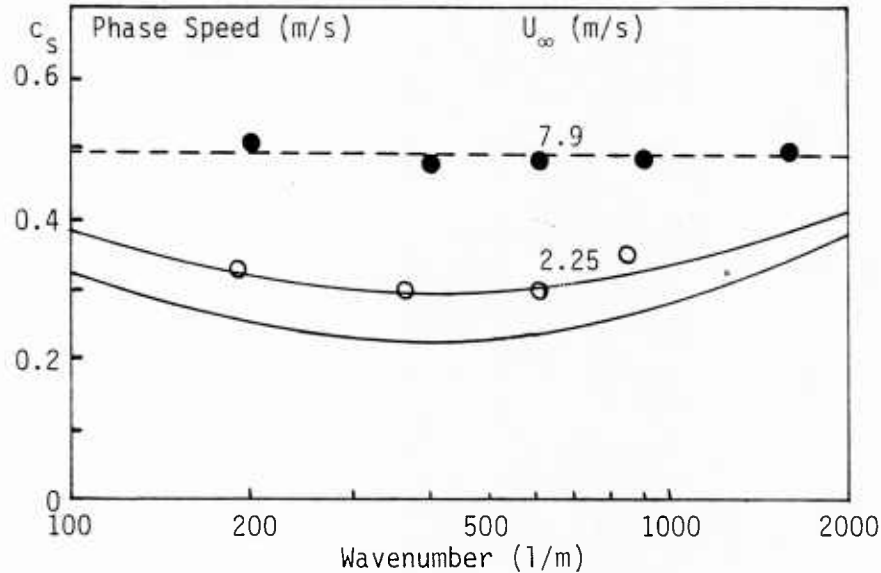


Figure 6.7 Phase speed versus wavenumber, Wright and Keller [28].

Wave gauge measurements were also made by Ramamonjiarisoa et al. [16] in a large wind-wave flume. Figure 6.8 shows typical phase speed data compared to theory (solid line). Dispersion is evident only below 3 Hz.

In addition, frequency spectrum measurements were made as a function of fetch, X . The spectra are sketched in Figure 6.9. For very short fetch X , the frequency spectrum shows a single line near 16 Hz, which increases in amplitude up to 1 m fetch. This is consistent with highly periodic ripples (catspaws). The fronts of these ripples evidently tend to steepen and the spectrum at 1 m shows a clear harmonic at 32 Hz, which is expected for such a distorted waveform. In this régime, the cascade of energy is clearly toward higher frequencies. One may think of this as a cross modulation of wind and wave effects. However,

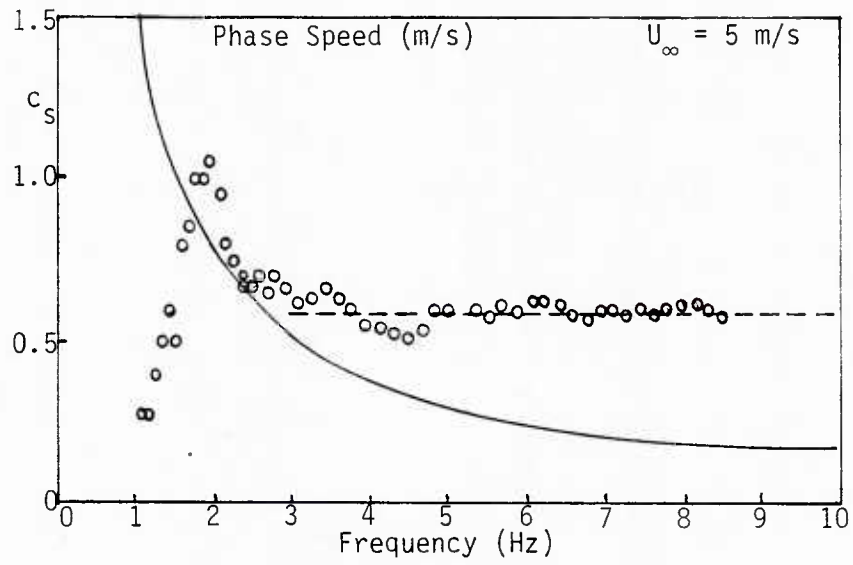


Figure 6.8 Phase speed measurements, Ramamonjiarisoa et al. [16].

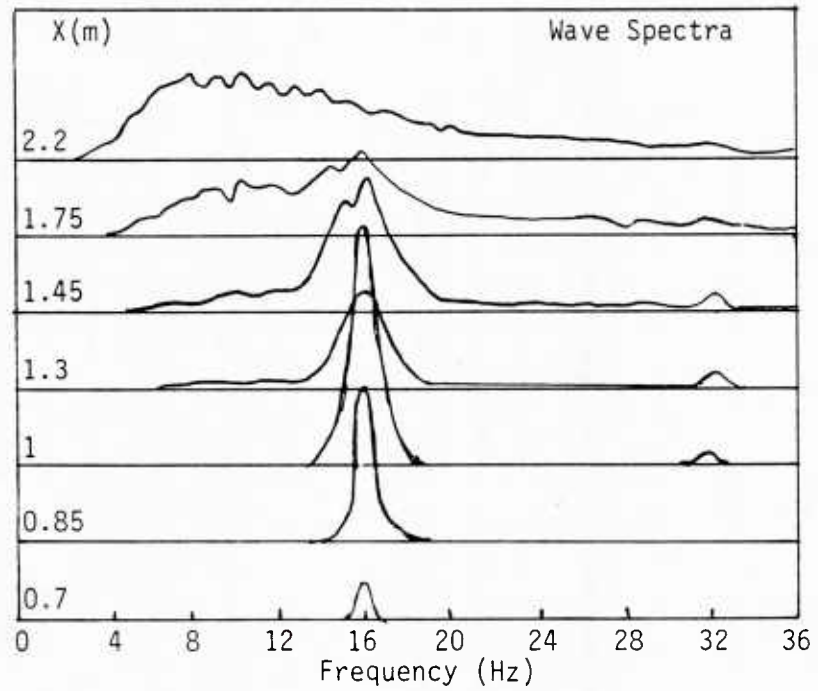


Figure 6.9 Wave spectra versus fetch X , Ramamonjiarisoa et al. [16].

the 16 Hz line no longer increases in amplitude beyond 1 m. Instead, it broadens, and lower-frequency energy begins to appear below 16 Hz. This indicates that there must be a cascade of energy in the reverse direction as well.

A chaotic process is a plausible explanation for the generation of big waves by little ones. In the initial phase, one would expect to see a weak subharmonic at exactly half the ripple frequency, i.e., 8 Hz; however, rapid degeneration of the system can cause broadening of both the subharmonic and the 16 Hz fundamental. As the wave grows and the amplitude reaches a critical point, the surface becomes unstable, destroying all the initial periodicity. This would explain the continuous spectrum seen at 2.2 m fetch.

At short fetch, the ripple waveform simply becomes distorted. Figure 6.10 is a sketch of a typical waveform photograph made in a small tank by Schooley [38] for a mean wind speed of 10 m/sec. In this stage, the ripples are highly periodic and only one cycle of the continuous wavetrain is displayed.

The waveform illustrates the typical distortion caused by non-linear steepening. The arrow at the front indicates the direction of water flow. The shock-like wavefront is also preceded by a small "capillary" ripple. This phenomenon can be readily observed in small tidal pools under conditions of high wind. However, the effects then are due to

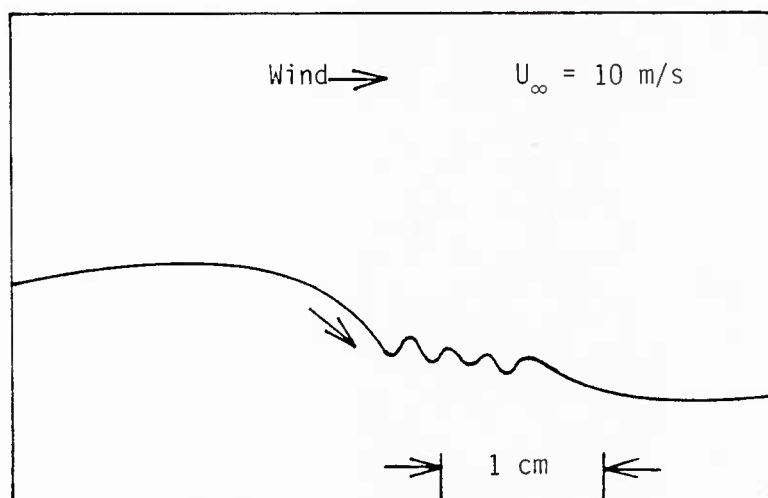


Figure 6.10 Surface waveform, Schooley [38].

shallow water, which is not the case above (which is now believed to be a drift-layer phenomenon, cf. Sec. 2).

Growth of steep wavefronts requires some type of nonlinear amplitude effect. The waveform of Figure 6.10 is clearly similar to gravity waves in shallow water, where the bottom causes an overtaking effect that can eventually lead to breaking. However, in the case of small-scale waves, capillary attraction is evidently sufficient to keep the wave from actually breaking. Banner and Phillips [39] refer to this phenomenon as "micro-breaking" and point out its significant rôle in the exchange of momentum between wave and wind.

Shemdin [15] proposed surface drift, illustrated in Figure 6.11, as the most likely nonlinear mechanism to account for wavefront steepening. Just as gravity waves steepen when they feel the bottom, waves traveling on a moving water layer steepen when they feel the effects of the slower water below. The drift layer can be approximated by an exponential decaying current with peak magnitude about 2-4% (or 1-5%) of wind speed and an effective thickness (h_e) of the order of millimeters in thickness [cf. Sec. 2.3].

Nonlinear waves in a periodic system evidently encounter a potential well that stalls the advance of small-scale disturbances at the wavefront. A periodic steep-fronted wave consists of harmonics of the fundamental. Their growth involves a cascade of energy to higher wave-numbers, and this does not explain how the sea develops.

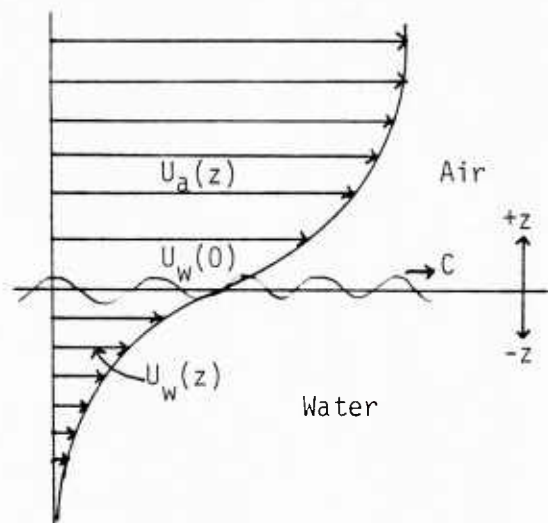


Figure 6.11 Drift layer motion, Shemdin [15].

Transfer of energy from wind to surface waves is, evidently, a high wavenumber phenomenon. A second mechanism, involving a cascade of energy in the reverse direction, is needed to explain the generation of low wavenumber energy. The most likely mechanism appears to be a similar transfer between the surface waves and the wind. Wave motion can no longer be considered "free" if it modulates the wind force that generates it. Initially, this type of feedback will produce subharmonics. However, if the surface becomes unstable in the process, all periodicity will disappear and the wave motion will become chaotic. Transfer of energy from higher to lower wavenumbers is typical of chaotic systems.

6.2 A Proposed Qualitative Wind-Wave Surface Model

The qualitative model of the build-up of the wind-driven sea, proposed by Middleton and Mellen [3], is illustrated in Figure 6.12. The four stages of wave development are:

- a. Initiation of linear periodic ripples (catspaws) at 16 Hz near the frequency of minimum phase speed.

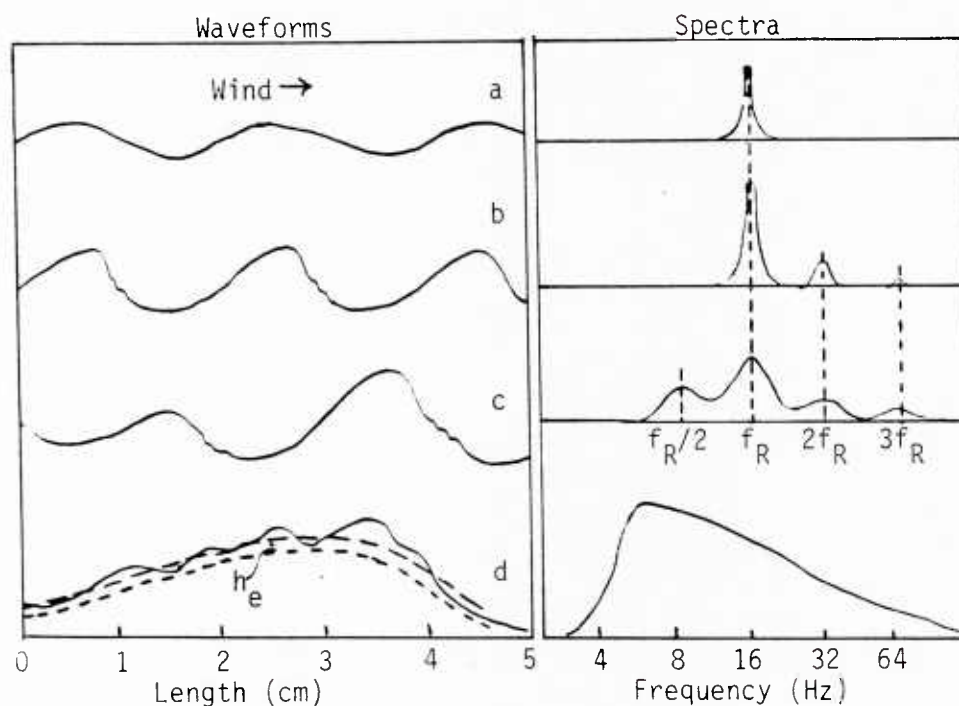


Figure 6.12 Wind-driven sea surface model, Middleton and Mellen [3].

- b. Development of surface drift, causing nonlinear steepening of the wavefronts. Propagation speed increases without dispersion. Cascade of energy is toward higher wavenumbers.
- c. Intermodulations between wind and water waves due to surface instability. Destruction of periodicity resulting in cascade of energy to lower wavenumbers.
- d. Final equilibrium state. Growth of longer gravity waves ceases because they travel faster and outrun their source. Smaller disturbances, continually generated on the surface, are no longer stable and decompose into sets of hydraulic "bumps" or solitons. Incoming wind energy is finally balanced by dissipation and the surface remains in equilibrium with continual development and decay of solitons.

After the wave-wind interactions are sufficiently well developed, small-scale disturbances generated on the surface have no periodic "potential wells" to trap them. Because of the resulting instability, they will decompose into elemental solitons or hydraulic "bumps" with specific amplitude and length relationships. The surface-drift layer provides a nonlinear balance, so that individual solitons propagate nondispersively. The proposed theoretical soliton model is described in Part I. Viscosity is neglected here, although it becomes an important effect in the later equilibrium stage. Surface tension effects, however, are specifically included.

7. Dispersion II: Mean Doppler Shift

We have developed two soliton-surface models so far: Model I, earlier [1], [2], without the effects of surface tension, i.e., $J = 0$, and Model II, where $J > 0$, in the present study. The significant features of each may be briefly summarized.

Model I: $J = 0$:

When surface tension is neglected, in effect $J = 0$, the result is that

$$\gamma_e = 0, \quad (2.11b); \quad \sigma_J \rightarrow \sigma_0 = c_0 h_e^2 / 6, \quad \text{cf. (2.2)}, \quad (7.1)$$

the governing KdV equation is (2.1), and only the soliton condition (2.26) is in force. There is no minimum thickness $h_{e-\min}$, and wavelength $\lambda_0 = \eta L_0 = 8b\{\sqrt{g} h_e^{5/2}/3v_0\}^{1/2}$, cf. (2.24b), with $\eta b = \sqrt{8}$ again, cf. (2.28), but now arbitrarily, such that $\hat{\lambda}_0$ is still defined between about the 2% of maximum points, as suggested by Lighthill [[9], Eq. (100), cf. (2.20)]. Correspondingly, there is also no minimum value of c_0 ($= \sqrt{gh_e}$). In Model I the soliton speed is $c_s = c_0 + v_0$, but c_0 is not taken to be the mean surfact drift speed $\overline{v_d}$, cf. (6) of Sec. 4.

Model II, $J > 0$:

Here $J=72.75$ dynes/cm (>0 at 20°C), $\sigma_J > 0$, cf. (2.3), channel thickness h_e has a minimum, cf. (2.30a), and the governing KdV equation is now given by (2.1a). This newer model is the one which we consider principally here (Secs. 2-4), as it is physically more meaningful and complete. In addition, it is important to note that in this model the channel propagation speed $c_0 \doteq v_d$, so that soliton speeds are $c_s = c_0 + v_0 = \overline{v_d} + v_0$, again with $c_0 \gg \overline{v_0}$, so that $c_s \doteq \overline{c_s} = \overline{v_d} + \overline{v_0}$ here, cf. (6) of Sec. 4.

Calculations of mean doppler shift, δf_0 , based on the "classical" relations (cf. Bass, Fuks, et al., [34], for example) and soliton Models I and II are now compared with the data [6] of Fig. 7.1. In particular, note the nondispersive nature characteristic of the soliton surface, i.e., $|\delta f_0| \sim f_0$, of the empirical data vis-à-vis that of the classical model, which is noticeably distant from the data for realistic wind speeds, i.e., $\overline{v_d} = 1-3\%$ of $10 \text{ m/s} = 10-30 \text{ cm/s}$, say. [The size of the circles is a measure of the error.]

The theoretical expressions for mean doppler shift (downwind) for the soliton (Sec. 3 of [2]) and Bass and Fuks models [32], [34] explicitly by

$$\text{Model I: } \delta f_0 = - \frac{2 \sin \theta_{0T}}{\lambda_0} \{ \overline{c_s} + \overline{v_c} \sin \phi_c + \overline{v_d} \sin \phi_w \}, \quad (7.2)$$

$$\text{Model II: } \delta f_0 = - \frac{2 \sin \theta_{0T}}{\lambda_0} \{ \overline{c_s} + \overline{v_c} \sin \phi_c \}, \quad (7.3)$$

where now in Model II $c_s \rightarrow \overline{c_s} = \overline{v_d} + \overline{v_0}$, as explained above. The "classical"

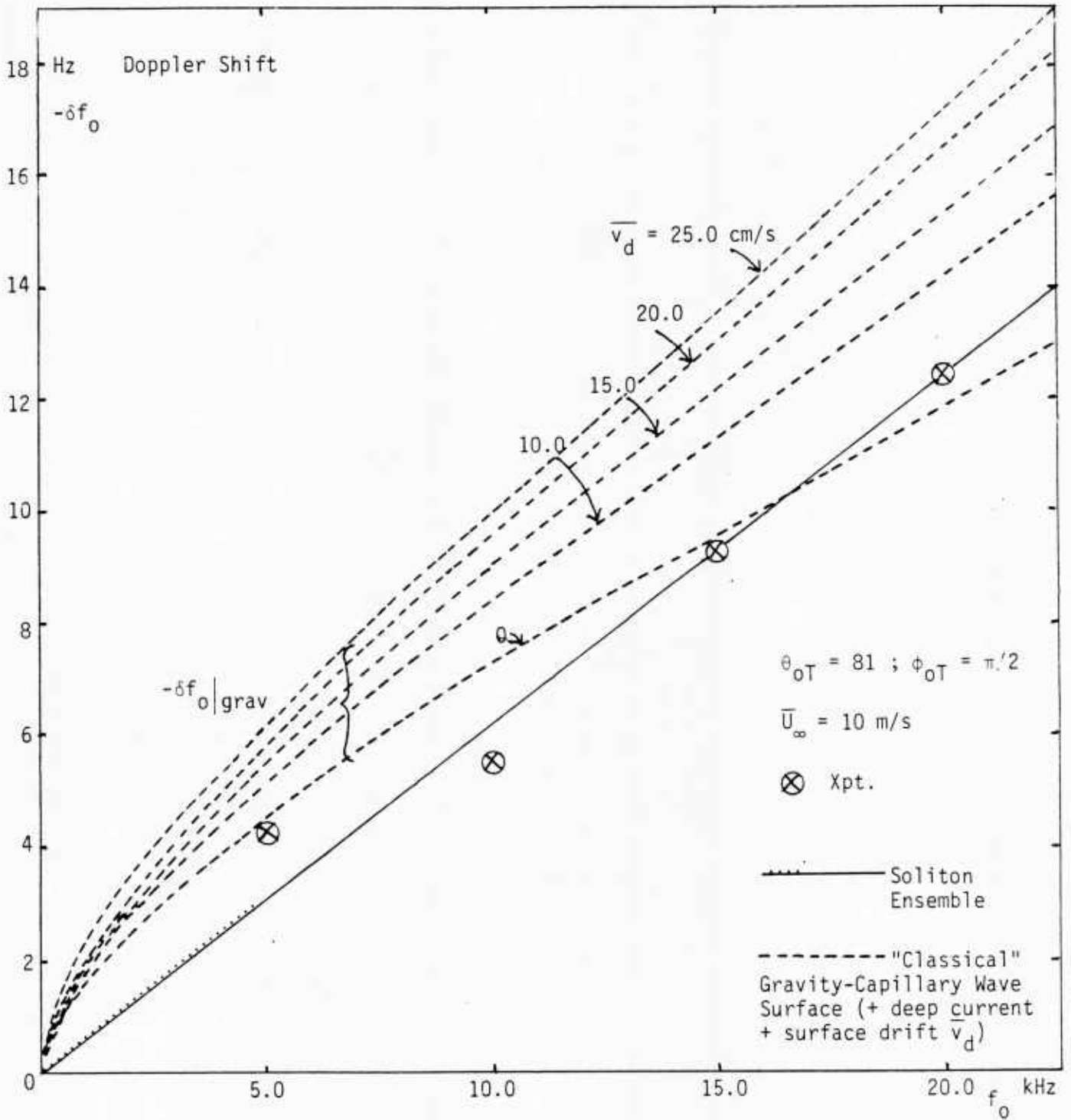


Figure 7.1 Doppler shift $-\delta f_0$, as a function of frequency, for the soliton Models I, II, Eqs. (7.2), (7.3), and the classical model, Eq. (7.4), including surface drift and deep current speeds. Theory (Middleton, [2], Sec. 3) and experiment, from the data of Roderick et al. [6].

expression for the mean doppler shift (on neglecting the capillary terms, since $\lambda_0 > 1$ cm) is

$$\delta f_0 \doteq - \left\{ \sqrt{\frac{g \sin \theta_{OT}}{\pi \lambda_0}} + \frac{2 \sin \theta_{OT}}{\lambda_0} (\bar{v}_c \sin \phi_c + \bar{v}_d \sin \phi_w) \right\}. \quad (7.4)$$

For the particular experiments involved here [6], \bar{v}_c = mean drift current = 26 cm/s, $\phi_c = 51.5^\circ$, $\phi_w = 116^\circ$; ($\phi_{OT} = \pi/2$, $\theta_{OT} = 81^\circ$, $\phi = 9^\circ$ grazing angle, cf. Fig. 5.1). (Mean surface drift speed \bar{v}_d was not measured.) Also, from the ensemble of measured δf_0 's it was found that $(\delta f_0)_{exp} = 12.4$ Hz at $f_0 = 20$ KHz (or $\lambda_0 = 7.5$ cm). Since, from (7.2), (7.3)

$$|\delta f_0| = \left| \frac{2 \sin \theta_{OT}}{\lambda_0} \right| |\bar{v}_{OD}|_{exp} \quad \therefore \bar{v}_{OD}|_{xpt} = 47.0 \text{ cm/s} \quad \left. \vphantom{|\delta f_0|} \right\} (7.5)$$

$$= \{ \} \text{ of (7.2), (7.3).}$$

For Model I the inferred soliton parameters are, cf. [2], shown in Table 7.1 (cf. Table 3.1 of [2]):

Table 7.1 Soliton Parameters of Model I

\bar{v}_d (cm/s)	c_s (cm/s)	h_e (cm)	v_o (cm/s)
10	17.7	$3.2 \cdot 10^{-1}$	$9.7 \cdot 10^{-2}$
15	13.2	$1.8 \cdot 10^{-1}$	$2.3 \cdot 10^{-2}$
20	8.7	$7.7 \cdot 10^{-2}$	$2.7 \cdot 10^{-3}$
25	4.2	$1.8 \cdot 10^{-3}$	$7.2 \cdot 10^{-5}$

In the moving current coördinate system, soliton speed becomes $\bar{c}_s = \bar{v}_d \sin \phi_w + c_o + v_o \doteq 27$ cm/s. Adding the current component $\bar{v}_c \sin \phi_c = 20.3$ cm/s gives the relative propagation speed ≈ 47 cm/s, which is in reasonable agreement with other experimental values $\approx (50-60$ cm/s), cf. Figs. 6.7, 6.8. We note that $h_e = O(1-3$ mm) here, much less than the h_{e-min} required in Model II, cf. (2.30a). Moreover, c_s here is also less

than $c_{0-\min}$ (= 23.2 cm/s), as a result of our neglecting surface tension and considering the soliton speeds, c_s , as distinct from that of the surface drift speed. This is not done in Model II ff.

With Model II, on the other hand, the effects of surface tension are included, and thus (cf. (6) of Sec. 4), \overline{v}_d is c_0 , so that $\overline{c}_s = \overline{v}_d + \overline{v}_0 = |\overline{v}_{0D}|_{\text{xpt}} - \overline{v}_c \sin \phi_c = 47.0 - 20.3 = 26.7$ cm/s. Since \overline{v}_d was not observed, we can only conclude from the constraints noted in Eq. (2.30a) that $[23.2 < c_0 < 26.7 - \overline{v}_0]$ cm/s, and $[0.55 < h_e = c_0^2/g < 0.73]$ cm. Accordingly, $[3.5 > \overline{v}_0 > 0+]$ cm/s, and if $\overline{v}_d = 2.5\%$ of $U_\infty = 10$ m/s, e.g., 25 cm/s, then $\overline{v}_0 = 1.7$ cm/s ($\ll c_0$), a not unreasonable value, along with effective layer thickness $O(7-8$ mm). For example, from the data of Fig. 5.2 in (2.26), we see that for $\sigma_S \sim 2$ cm, $\sigma_h / L_0 \sim 5$ cm, $h_e = 0.73$ cm, Eq. (2.26) is well satisfied. Of course, further experiment is needed, to determine both h_e and \overline{v}_0 , in addition to the primary task of direct, as opposed to the present inferential, experimental establishment of the soliton model itself.

8. Doppler Spread

The Doppler spread for the soliton and classical models are shown in Figure 8.1. Spread is measured at the $10 \log_{10} e^{-1}$ points of the spectrum. The "classical" model B/F (solid line) [32], [34] is given by

$$\Delta f_{B/F} \approx 1 \cdot 10^{-3} f_0 \quad (8.1)$$

For the soliton models [2] (curve 1), the spread is given by

$$\Delta f_S \approx [(A^2 + B^2) f_0^2 + D^2]^{1/2}, \quad (8.2)$$

where the term A accounts for phase modulation by large-scale gravity waves, B accounts for the variations in soliton velocities, and D is a frequency-independent random amplitude modulation correction arising from variations in slope due to large-scale gravity waves. The data curve-fit values are $A = 3.3 \cdot 10^{-4}$, $B = 7.8 \cdot 10^{-4}$, and $D = 15$. The dashed lines 2 and 3 show the effects for $D = 0$ and $B = D = 0$, respectively.

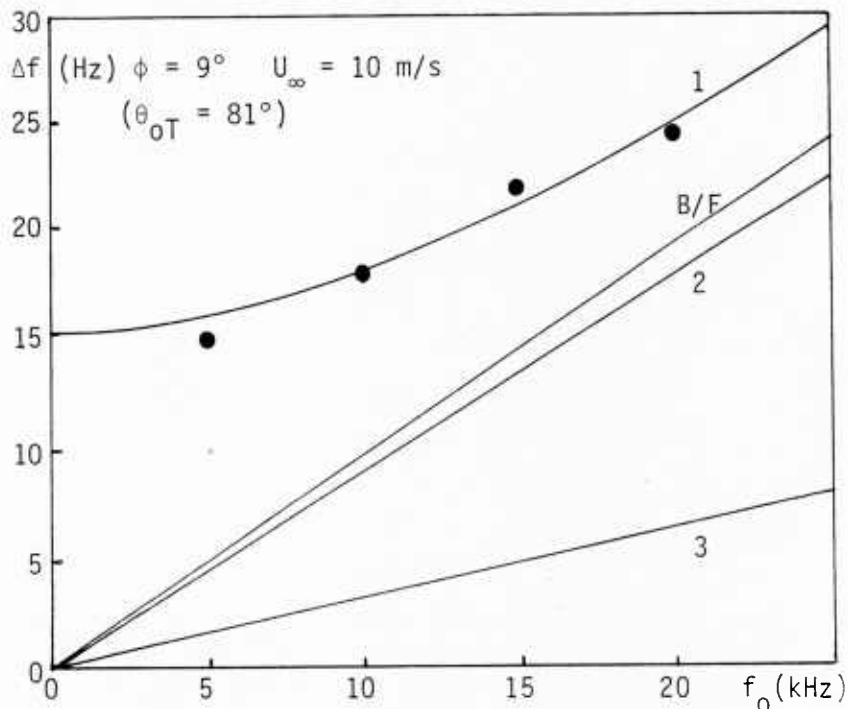


Figure 8.1 Doppler spread Δf versus frequency (Middleton [2], Sec. 4).

It is evident that, for small grazing angles and low frequencies, the soliton model ascribes most of the doppler spread to B and D. At larger frequencies, the phase modulation term A becomes dominant and the two theories come closer together, but nevertheless remain asymptotically quite distinct ($O(\Delta f = 5 \text{ Hz})$). It should be remarked, however, that ΔF does not depend explicitly on the soliton mechanism, since the explicit form of the surface soliton covariance K_S , (3.12), is not needed for determining doppler spread (see Sec. 8 of [2]). Only if the spectrum of the scattered return is required, or the backscatter intensity, is K_S explicitly needed, as is the case in the preceding analysis.

9. Conclusions

We summarize the principal results reflecting on the validity of the proposed soliton surface model. The mathematical details are described in Part I (Secs. 2-4), and the experimental support is presented in Part II (Secs. 5-8).

The present models, including [1], [2] based on soliton theory [10], describe essentially all of the known scattering phenomena at small grazing angles, high frequencies in bubble-free régimes, and for suitable surface wind conditions, with mean wind speeds, U_∞ , above $O(2-4 \text{ m/s})$, cf. [28]. By adding a distinct component of roughness vis-à-vis the underlying single gravity-capillary wave surface to the surface-wave spectrum, the theoretical backscattering strength and doppler statistics all become consistent with experiment. Furthermore, the existence and behavior of the added component do not violate the known properties of the sea surface in any way. In fact, it appears to be a necessary condition on all counts. Critical to the soliton theory here is the existence of a thin, wind-drift surface layer (or channel) which permits the generation of solitons as described by the KdV equation.

The soliton hypothesis presented here and extended to include the limiting effects of surface tension, cf. (2.1a), is a plausible mechanism for all the hydrodynamic phenomena involved. The evidence from scattering and wave-gauge measurements points to specific characteristics of the small-scale roughness, and the soliton appears to be the only kind of wave that can satisfy all requirements. The hydrodynamic effects are similar to water flowing down an inclined plane where nonlinearity causes the formation of hydraulic "bumps" with irregular wavefronts. On the sea surface, the velocities depend on local conditions of both the wind and the surface slope. Doppler shift reflects the mean speed in the downwind direction. The soliton hypothesis, for which propagation is nondispersive, is consistent with doppler measurements in detail. With reasonable physical assumptions relative to the soliton component (cf. Secs. 3 and 4 above), predictions of both spread and shift of the spectra can be put into very good agreement with experiment. This is in addition to accounting for the discrepancy in backscatter cross sections noted originally [1]-[3], [5]-[8], and Sec. 5 here.

Wave spectra, either measured or inferred from Doppler measurements, show no dispersion at high frequencies, cf. Secs. 5-7. The "dispersion" relation becomes $\sigma_S \approx g/2\pi f_S$ for low frequencies (gravity régime) and $c_S \approx \text{constant}$ for high frequencies (nonlinear régime). The wavenumber spectra are then asymptotic to K^{-4} in both régimes. However, the spectrum levels can be much greater at high wavenumbers, depending on the

wind conditions. The spectrum, therefore, tends to be saturated only in the low-wavenumber régime. Greater levels at high wavenumbers are required to explain the increase in scattering strength, as noted in Sec. 5.

With the supporting evidence of the wave-gauge spectrum data, [16], [20],[21], it seems clear that the extra roughness at high wavenumbers truly exists. From the theoretical standpoint, the soliton mechanism appears to be the most plausible one. See, in particular, Sec. 5 of [2] for an additional comparison of models.

However, a number of questions remain to be answered. Full justification of the model requires more detailed knowledge of both the parametric dependence on wind conditions as well as the hydrodynamics involved. Proposed experimental and theoretical investigations, addressed to these questions, are outlined in Sec. 5 of [8], TD-7583. Specifically, the explicit, as distinct from the presently inferred, existence of the soliton surface needs to be demonstrated.

REFERENCES

- [1]. D. Middleton, "Acoustic scattering cross sections for truly composite wind-wave surfaces: I. Scattering without bubbles," NUSC Tech. Doc. 7205, August 1984, New London, CT 06320.
- [2]. _____, "Acoustic scattering cross sections for truly composite wind-wave surfaces: II. Backscatter cross sections and Doppler effects at high frequencies and small angles for 'bubble-free' régimes," NUSC Tech. Report TR-7635, July 22, 1986, New London, CT 06320.
- [3]. D. Middleton and R. H. Mellen, "Wind-generated solitons: A potentially significant mechanism in ocean surface wave generation and surface scattering," IEEE J. Oceanic Engineering 10, No. 4, October 1985, pp. 471-476.
- [4]. L. Brekhovskikh and Yu. Lysanov, Fundamentals of Ocean Acoustics (Springer Series in Electro-Physics No. 8), Springer-Verlag (New York), 1982, p. 23 and Sec. 1.6.
- [5]. S. T. McDaniel and A. D. Gorman, "Acoustic and radar sea-surface backscatter," J. Geophysical Res. 87, 4127-4136 (1982). (See also refs. [1], [2] here.)
- [6]. W. I. Roderick and J. B. Chester, R. K. Dullea, "High-frequency acoustic backscatter from the sea surface," NUSC Tech. Doc. 7183, July 12, 1984, New London, CT 06320.
- [7]. _____, "Project WEAP," NUSC Project No. A67001, W. I. Roderick, as P.I., since 1982 - .
- [8]. R. H. Mellen, D. Middleton, and J. W. Fitzgerald, "Sea surface backscattering and the soliton mechanism," NUSC Tech. Doc. TD-7583, Feb. 21, 1986, NUSC, New London Laboratories, New London, CT 06320. This is based directly on a Final Report, Planning Systems, Inc. (same title, prepared for NUSC under Contract N66604-85-B097, Sept. 30, 1985).
- [9]. J. Lighthill, Waves in Fluids, Cambridge University Press, 1979, pp. 463-468.
- [10]. R. K. Dodd, J. C. Eilbeck, J. D. Gibbon, and H. C. Morris, Solitons and Nonlinear Wave Equations, Academic Press (New York), 1982.

- [11]. A. C. Scott, F.Y.F. Chu, D. W. McLaughlin, "The soliton: A new concept in applied science," Proc. IEEE, Vol. 61, No. 10, pp. 1443-1483, Oct., 1973.
- [12]. A. Korpel and P. P. Banerjee, "A heuristic guide to nonlinear dispersive wave equations and soliton-type solutions," Proc. IEEE, Vol. 72, No. 9, pp. 1109-1130, Sept., 1984.
- [13]. G. E. Peterson, "Electrical transmission lines as models for soliton propagation in materials: Elementary aspects of video solitons," Bell Syst. Tech. J. 63, pp. 901-909, 1984.
- [14]. M. Olsen, H. Smith, and A. C. Scott, "Solitons in a wave tank," Am. J. Phys. 52, pp. 826-830, 1984.
- [15]. O. H. Shemdin, "Wind-generated current and phase speed of water waves," J. Phys. Oceanography 2, pp. 411-419, 1972.
- [16]. A. Ramamonjiarisoa, S. Baldy, and I. Choi, "Laboratory studies on wind-wave generation, amplification and evolution," in Turbulent Fluxes Through the Sea Surface, ed. A. Favré and K. Hasselmann, Plenum Press (New York), 1978, pp. 403-420.
- [17]. S. T. McDaniel and A. D. Gorman, "Examination of the composite-roughness scattering model," J. Acoust. Soc. Am. 73, No. 5, pp. 1476-1486, May 1983.
- [18]. G. P. deLoor, "Project Nordwijk, Part III: The radar backscatter coefficient as measured at Platform Nordwijk and comparison with other data," National Defense Research Organization TNO, The Hague, Netherlands, Report PHL 1982-22, May 1982.
- [19]. R. T. Lawner and R. K. Moore, "Short gravity and capillary wave spectra from tower-based radar," IEEE J. Oceanic Eng. OE-9, pp. 317-324, 1984.
- [20]. H. Mitsuyasu and T. Honda, "The high-frequency spectrum of wind-generated waves," J. Oceanographic Soc. Japan 30, pp. 185-198, 1974.
- [21]. H. Mitsuyasu, "Measurement of the high-frequency spectrum of ocean wave surfaces," J. Phys. Oceanogr. 7, pp. 882-891, 1977.

- [22]. D. Middleton, "Space-Time Processing for Weak Signal Detection in Non-Gaussian and Non-Uniform Electromagnetic Interference (EMI) Fields," ITS/NTIA Contractor Report 86-36, Feb., 1986, U.S. Department of Commerce, 325 Broadway, Boulder, CO 80303.
- [23]. _____, "Second-order nongaussian probability distributions and their applications to 'classical' nonlinear processing problems," Proceedings of 1986 "Conference on Information Sciences and Systems," March 19-21, 1986.
- [24]. I. S. Gradshteyn and I. M. Ryzhik, Table of Integrals, Series, and Products, 4th Ed., Academic Press (New York), 1980.
- [25]. D. Middleton, An Introduction to Statistical Communication Theory, McGraw-Hill (New York), 1960.
- [26]. G. N. Watson, Theory of Bessel Functions, McMillan (New York), 1944.
- [27]. S. A. Kitaigorodskii, The Physics of Air-Sea Interaction, Israel Program for Scientific Translations, NTIS, Springfield, VA; Vol. TT-72-50062, 1973.
- [28]. J. M. Wright and W. C. Keller, "Doppler spectra in microwave scattering from wind waves," *J. Physics of Fluids* 14, pp. 466-474, 1971.
- [29]. C. S. Cox and W. H. Munk, "Measurement of the roughness of the sea surface from photographs of the sun's glitter," *J. Opt. Soc. Amer.*, Vol. 44, No. 11, pp. 838-850, 1954.
- [30]. N. N. Galubin, *Akus. Zhur.* 22, 343-350, 1976; English Transl.: *Soviet Physical Acoustics* 23, pp. 193-197, 1976. See Fig. 1.26 of [4], refs., and text.
- [31]. B. F. Kur'yanov, "The scattering of sound at a rough surface with two types of irregularity," *Soviet J. of Physical Acoustics* 8, No. 3, pp. 252-257, 1962; in English, 1963. See [32], Chapter 10 and bibliography therein.
- [32]. F. G. Bass and I. M. Fuks, Wave Scattering from Statistically Rough Surfaces (trans. and ed. by C. B. and J. F. Vesecky), Pergamon Press (New York), 1979.

- [33]. W. L. Pierson and L. Moscovitz, "A proposed spectral form for fully developed seas based on the similarity theory of S. A. Kitaigorodskii," *J. Geophys. Res.* 69, pp. 5180-5190, 1964; see also [27].
- [34]. F. G. Bass, I. M. Fuks, A. I. Kalnikov, I. E. Ostrovsky, and A. O. Rosenberg, "Very high frequency radiowave scattering by a disturbed sea surface," *IEEE Trans. Antennas and Propagation*, Vol. AP-16, pp. 554-568, 1968.
- [35]. R. H. Mellen, "Doppler shift of sonar backscatter from the sea surface," *J. Acous. Soc. Amer.* 36, pp. 1395-1396, 1964.
- [36]. W. L. Konrad, D. G. Browning, and R. H. Mellen, "Doppler spectra of sea-surface backscatter at high acoustic frequencies," NUSC TR 6735, July 1982, NUSC, New London, CT 06320.
- [37]. H. Boehme, "Measurement of acoustic backscattering from very rough water surfaces," *J. Acous. Soc. Amer.* 65, pp. 350-359, 1979.
- [38]. A. H. Schooley, "Profiles of wind-created water waves in the capillary-gravity transition region," *J. Fluid Res.* 16, pp. 100-108, 1958.
- [39]. M. L. Banner and O. M. Phillips, "On the incipient breaking of small-scale waves," *J. Fluid Mech.* 65, pp. 647-656, 1974.
- [40]. E. J. Plate, "Wind-generated water surface waves: The laboratory evidence," in Turbulent Fluxes Through the Sea Surface, ed. A. Favré and K. Hasselmann, Plenum Press (New York), 1978, pp. 395-401.
- [41]. D. Middleton, "Acoustic Scattering by Wind-Generated Wave Surface Solitons: A Critical Summary," First IMACS Symposium on Computational Acoustics, Aug. 6-8, Yale University, New Haven; Proceedings (Spring, 1987), North Holland Pub. Co.
- [42]. B. B. Kadomtsev and V. I. Petviashvili, "Stability of Solitary Waves in Weakly Dispersive Media," *Dokl. Ak.-Nauk S(ibirisk)SSR*, Vol. 192, No. 4, 1970, pp. 753-756.
- [43]. A. S. Monin and V. P. Krasitskii, Ocean Surface Wave Phenomena, Gidrometevizdat (Moscow) USSR, 1985, esp. Chapters 2, 3.

INITIAL DISTRIBUTION LIST

Addressee	No. of Copies
NAVSEASYSKOM (SEA-63D (CDR E. Graham))	1
NORDA (Code 530; 113 (B. Adams, Dr. R. Farwell T. Goldsberry, Dr. M.Y. Su); 240 (Dr. N. Kinney)	6
NOSC (Code 013 (Dr. E. Cooper) (3); 7133 (Dr. C. Persons); 5322 (Dr. J. Northrup); (B. Smith); Marine Physical Labs (Dr. F. Fisher, Dr. F. Spiess))	8
SACLANTCTR (Tech. Director (R. Goodman))	1
ONR (Code 1125 UA (Dr. R. M. Fitzgerald, Dr. R. Sternberg); 1125 AR (R. Obrochta); 1111 SP (Dr. N. Gerr); 111 (Dr. T. Berlincourt); 112 (G. Hamilton); 1122B (E. Hartwig); 1111 (Dr. E. Wagman, Dr. Ringison))	9
NRL (Code 5160 (E. Franchi); Code 5303 (Dr. L. Wetzel))	2
ITS/NTIA (U.S Dept. of Commerce (Dr. A. Spaulding, Dr. C. Rush))	2
ARL, UNIV OF TEXAS (G. Wilson, G. Ellis, Prof. C. Horton, Dr. H. Boheme, Dr. R. Culbertson)	5
DTIC	12
NAVPGSCOL (Prof. H. Medwin; Library)	2
SAIC (W. Chadsey, Dr. Tatrow, Dr. J. Brackett Hersey, Dr. R. Green)	4
YALE UNIVERSITY (Prof. P. H. Schultheiss)	1
Scripps Inst. of Oceanography, La Jolla, CA (Dr. W. Munk)	1
ARL/PENN STATE, STATE COLLEGE, PA (Dr. S. McDaniel, Dr. D. McCammon, Dr. F. Symon)	3
CYBERLINK, Boulder, CO (Dr. P. McManamon)	1
APL, Johns Hopkins (Dr. J. Apel)	1
WPL-NOAA (Wave Propagation Lab (Dr. S. Clifford, Dr. Derr))	2
NOAA (Dir. of NOAA Labs, (Dr. J. Apel))	1
Johns Hopkins Univ. (Dept. of Oceanography (Prof. O. M. Phillips))	1
UNIV OF WISCONSIN (Dept. of Geophysics (Prof. C. S. Clay))	1
UNIV OF NEW MEXICO (Dept. of Elec. Eng. (Prof. D. P. Petersen))	1
PSI, Inc. (Dr. R. H. Mellen, J. W. Fitzgerald)	2
UNIV OF MIAMI/RSMAS (Dr. F. D. Tappert)	1
Dr. David Middleton, New York, NY	15
APL/UW, (Dr. E. Thorsos, Dr. R. Jackson, S. McConnell)	3
ONT (T. Warfield, T. Kooij, B. Palmer)	3
NADC (Code 3042 (T. Polaneczky))	1
UNIV OF ILLINOIS (V. P. Twerski)	1
FWG/Kiel, Germany (Dr. H. Herwig, Dipl. B. Nuetzel)	3
UNIV OF KANSAS (R. T. Moore, R. K. Moore)	2
SONALYSTS, Inc. (W. D. ...)	2
UNIV OF WASHINGTON (Dept. of ... Eng. and App. Math (Prof. A. Ishimaru))	2
UNIV OF NEBRASKA (Dept. of ... ng. (Prof. E. Bahar))	1
DARPA (C. Stewart)	1
NCSC (Dr. L. J. Satkowiak)	1
RAYTHYEON (S. Ehrlich)	1
SAI Space Systems Operations (Dr. R. Becherer)	1

U228982

